POLITECNICO DI TORINO
Repository ISTITUZIONALE

Silanized and Cu-doped bioactive glass as filler for biobased photocurable 3D printed scaffolds

Original
Silanized and Cu-doped bioactive glass as filler for biobased photocurable 3D printed scaffolds / Bergoglio, M., Najmi, Z., Cochis, A., Miola, M., Vernè, E., Sangermano, M.. - In: MATERIALS TODAY CHEMISTRY. - ISSN 2468-5194. - 44:(2025), pp. 1-16. [10.1016/j.mtchem.2025.102559]

Availability:
This version is available at: 11583/2997406 since: 2025-02-10T11:18:48Z

Publisher:
Elsevier

Published
DOI:10.1016/j.mtchem.2025.102559

Terms of use:

This article is made available under terms and conditions as specified in the corresponding bibliographic description in the repository

Publisher copyright

(Article begins on next page)

18 November 2026

Materials Today Chemistry 44 (2025) 102559

Contents lists available at ScienceDirect

Materials Today Chemistry

journal homepage: www.journals.elsevier.com/materials-today-chemistry/

Silanized and Cu-doped bioactive glass as filler for biobased photocurable 3D printed scaffolds

Matteo Bergoglio [a], Ziba Najmi [b], Andrea Cochis [b], Marta Miola [a,*], Enrica Vernè [a], Marco Sangermano [a]

[a] Dipartimento di Scienza Applicata e Tecnologia, Politecnico di Torino, C.so Duca degli Abruzzi 24, 10129, Torino, Italy
[b] Department of Health Sciences, Center for Translational Research on Autoimmune and Allergic Diseases CAAD, Università Del Piemonte Orientale (UPO), 28100, Novara, Italy

ARTICLE INFO

Keywords:
Bio-based scaffold
3D printing
Photopolymer
Bioactive glass
Cu-doping
Silanization

ABSTRACT

This research explores and characterizes a photo-curable, biobased resin reinforced with bioactive glass (BGs) to produce scaffolds 3D-printed for tissue engineering applications. Through a sol-gel were synthesized two types of BGs, standard and copper-doped. The BGs were silanized to enhance resin compatibility. Transmission FTIR, photoDSC and photoreology fully characterized the UV-curing behaviour of the resin formulation. 3D-printed scaffolds' mechanical properties were evaluated through tensile tests and dynamic mechanical thermal analysis (DMTA). At the same time, morphology and dispersion of the BGs inside the polymer matrix were assessed utilizing Scanning Electron Microscopy (SEM). Bioactivity was evaluated by immersing the scaffolds in a simulated body fluid (SBF) to evaluate hydroxyapatite (HAp) formation. Antibacterial activity tests following the ISO 22196 protocol demonstrated 57 % fewer viable *Staphylococcus aureus* cells adhered to the surfaces of A7I3-sil and A7I3–Cu-sil compared to the control. SEM and 3D-reconstructed images showed reduced bacterial aggregations (from 13-14 % to 8–9%) and Z-maximum (from 4.5 μm to 2.5 μm). On the treated samples most bacterial cells appeared as single and sporadic cells, making them more easily removable with mild antibiotics.

This work aims to enhance bone scaffold design that combines mechanical strength with bioactivity using sustainable and biobased materials. The findings provide a foundation for future developments in tissue engineering.

1. Introduction

Bone damage and defects, particularly in the ageing population, are expected to increase over the years [1,2] man bone possesses outstanding self-healing properties [3,4], certain conditions require intervention beyond the natural body repair mechanism. For instance, approximately 13 % of fractures in the tibial bone result in delayed union or fracture non-union [5]. Furthermore, various orthopaedic conditions require extensive regeneration, which surpasses the body's natural self-healing capabilities. Bone grafting, bone implants and bone allografts have been employed over the years to address these challenges [6]. Since 1987, tissue engineering has become essential for bone repair and regeneration, utilizing biocompatible materials to support and stimulate cell growth, effectively mimicking the extracellular matrix [7].

In this context, bioactive glasses (BG) emerge as a significant innovation. Introduced by Larry Hench, BGs are a unique class of ceramic biomaterials used in both hard and soft tissue engineering. They offer excellent osteoconductive and angiogenic properties, crucial for bone repair [8,9]. Besides promoting bone regrowth, BGs also exhibit antibacterial properties. Antibacterial properties are attributed to localised pH increase derived from the release of glass-network ions when immersed in bodily fluids. Incorporating various metal ions, including silver, zinc, strontium, and copper enhances these antibacterial effects [10–12]. Copper, in particular, has been extensively studied for biomedical applications since it offers a dual role in promoting antimicrobial activity and facilitating tissue repair, including bone and skin regeneration [13,14]. However, introducing excessive Cu ions can negatively impact glass solubility and bioactivity, necessitating a careful optimisation [15,16].

* Corresponding author.
E-mail addresses: matteo.bergoglio@polito.it (M. Bergoglio), ziba.najmi@uniupo.it (Z. Najmi), andrea.cochis@med.uniupo.it (A. Cochis), marta.miola@polito.it (M. Miola), enrica.verne@polito.it (E. Vernè).

https://doi.org/10.1016/j.mtchem.2025.102559
Received 28 October 2024; Received in revised form 24 January 2025; Accepted 27 January 2025
Available online 8 February 2025
2468-5194/© 2025 The Authors. Published by Elsevier Ltd. This is an open access article under the CC BY license (http://creativecommons.org/licenses/by/4.0/).

Despite their benefits, BG-based scaffolds often lack sufficient mechanical properties, limiting their use, especially in load-bearing applications [17]. To overcome the limitation, composite materials that integrate BGs with polymers have been developed for various biomedical applications, enhancing mechanical performance and bioactivity [18]. Polymer-ceramic composite scaffolds have been manufactured using various methods, including moulding and casting, electrospinning, and additive manufacturing (AM) [19–22]. By selecting different polymeric matrices, the mechanical properties of the scaffold can be optimised, ensuring the requirements needed for a broad range of applications [23].

Among the manufacturing methods, AM process has gained attention in the field due to its ability to produce precise, patient-specific scaffolds for large bone defects using a layer-by-layer technique [24–30]. Different polymers, including natural or synthetic (e.g. hydrogel, proteins, thermoplastic elastomers), have been utilised in AM processes [31,32]. Photopolymers sensitive to UV-light are particularly promising for AM due to their crosslinked molecular structure, which imparts thermal resistance and exhibits minimal creep and stress relaxation [33,34]. Our group has extensively studied photopolymers, especially in the context of additive manufacturing [35–39]. The use of photo-curable polymers in AM goes into the category of VAT photo polymerisation (VP), a technique characterised by the fabrication of 3D manufacts starting from the liquid resin, added with a cationic or radical photoinitiator [40]. The photoinitiator can adsorb the irradiating light, starting the polymerisation reaction in a process much less important in energy dissipation than thermal curing [41–46]. VP is the most used method of digital light processing (DLP) since it can produce high-resolution patterns at room temperature through the use of a system of mirrors called digital mirror device (DMD) to direct UV light precisely [47]. Different kinds of thermoset polymers can be printed, both in a cationic photocuring exploiting epoxy ring [48,49] or radical curing, exploiting acrylate functionalities [50].

The growing demand for environmentally sustainable materials has shifted the focus to biobased alternatives to fossil-derived polymers in VP processes. Traditional fossil-based polymers, such as those based on Bisphenol A, both epoxy and acrylate products, are being replaced by biobased products [51,52]. Specifically, vegetable oils are renewable, cost-effective and potentially biodegradable [53,54]. These oils contain triglyceride chains with a high content of double bonds and hydroxyl groups that be converted into epoxy or acrylate groups for high-reactivity 3D printing [55–58]. Several studies have demonstrated the possibility of using acrylate derivatives from vegetable oils in 3D printing, with acrylate soybean oil particularly notable for its versatility [59–65].

Combining polymers with reinforcing phases like BGs can enhance scaffold performance, making them suitable for biomedical applications. Developing biobased polymeric composite through photopolymerization for 3D printing offers immense potential in this field [66–68]. The approach addresses the limitations of pure polymeric and BG scaffolds by improving mechanical stability and bioactivity [69–73]. A critical factor in achieving this is the interface between the polymer and the bioactive glass, which can be enhanced through silanization, improving the wettability of the BG and, consequently, the adhesion [74–79].

Based on our previous research on AESO-based polymeric scaffolds reinforced with bioactive glasses [47], this study aims to address the limitations of the developed scaffolds by manufacturing biobased polymeric composites with enhanced mechanical and biological properties. The AESO matrix is reinforced with two types of BGs synthesized by a sol-gel method: Si–Ca–P bioactive glass, named S4, and a novel Cu-doped variant to impart antibacterial properties. Moreover, we employed a silanization process on the BGs to enhance mechanical performance, improving the interface between the polymer matrix and the reinforcing ceramic phase.

The study investigates the effect of these novel Cu-doped BGs on the mechanical and biological properties of 3D-printed scaffolds. The synthesized BGs were dispersed into the UV-curable formulations, and the UV-curing process was investigated. Specifically, the impact of silanization and Cu doping on bioactivity, antibacterial performance, and the UV-curing process was considered, along with the 3D printing feasibility, emphasizing the potential of these materials for advancing biobased 3D-printed scaffolds in biomedical applications.

2. Materials and method

2.1. Materials

Acrylated soybean oil (AESO) isobornyl acrylate (IBOA), Phenylbis (2,4,6-trimethyl benzoyl) phosphine oxide. Ammonium hydroxide (NH_4OH), tetraethyl orthosilicate (TEOS), triethyl phosphate (TEP), calcium nitrate tetrahydrate ($Ca(NO_3)_2{\cdot}4H_2O$), 3-(Trimethoxysilyl)propyl methacrylate (TMSPMA), Copper(II) nitrate trihydrate ($Cu(NO_3)_2 \cdot 3H_2O$) were all obtained from Sigma Aldrich, Milano, Italy.

2.2. Bioactive glasses synthesis

In this study, two types of BGs were synthesized using a modified Stöber method and following our previous paper [50,80].

The synthesis began by mixing two different solutions while stirring. The first solution consisted of ammonium hydroxide (NH_4OH), bi-distilled water, and ethanol, while the second solution was made of ethanol (EtOH) mixed with tetraethyl orthosilicate (TEOS). The initial mixing of the solutions initiated the formation of silica (SiO_2) particles. Subsequently, triethyl phosphate (TEP) as the phosphorus (P) precursor and calcium nitrate tetrahydrate ($Ca(NO_3)_2{\cdot}4H_2O$) as the calcium (Ca) precursor were introduced to the mixture. The resulting system was then heated at 60 °C for 48 h to eliminate solvents, followed by furnace treatment at 700 °C for 2 h with a controlled heating ramp of 5 °C/min to remove any residual organic compounds.

The same method was used for the Cu-doped bioactive glass synthesis, with the addition of Copper (II) nitrate trihydrate ($CuN_2O_6{\cdot}3H_2O$) after incorporating the Ca precursor.

The composition of the obtained bioactive glass (S4) and the Cu-doped bioactive glass (Cu–S4) is reported in Table 1.

2.2.1. Bioactive glass silanization

To improve the bond between the polymeric matrix and the glass particles, thus enhancing the mechanical properties, a silanization process was carried out. The silanization of all types of BGs involved three different methods based on literature [78,79].

Initially, the –OH groups were activated to expose them for an effective silanization process. The activation involved 0.5 g of glass powder, previously disaggregated, and then immersed in 2 ml of acetone. The solution was placed in an ultrasound bath and centrifuged for 5 min at 7000 rpm after which the acetone was removed. The exact process was repeated with water instead of acetone three times, to ensure all traces of acetone were removed.

A solution of 20 % of TMSPMA in ethanol has been used for all the silanization methods. The first method involved mixing the glass powder with a magnetic stirrer for 2 h. The second method also involved 2-h mixing, but acetic acid kept the solution at a pH of 5. The third method involved mixing the solution for 24 h. All methods included a

Table 1
Nominal composition of bioactive glass S4 and bioactive glass Cu-doped CuS4.

	Composition %wt			
Bioactive glass name	SiO_2	P_2O_5	CaO	CuO
S4	77	9	14	–
Cu–S4	77	9	9	5

subsequent centrifugation step at 7000 rpm for 2 min to remove the solution and any remaining silanol that was not successfully bonded to the glass surface. As a final step, the glass was dried in an incubator at 37 °C for 24 h.

2.3. Formulation and photo-curing

Following our previous work, the bio-based resin was combined with 30 % bio-derived reactive diluent (IBOA) and 1phr (per hundred resin) of a radical photo-initiator. Based on previous studies, the photo-curable resin formulation was combined with 30 phr of BGs [50]. The mixtures were homogenized employing an ultra-turra T10 basic until the homogenization of all the components. To complete and ensure the process, the resins were further processed using an ARE-310 Thinky mixer (Laguna Hills, USA) with a cycle composed of 3 min of mixing followed by 3 min of defoaming, repeated three times.

Nine formulations were developed, and their compositions are presented in Table 2. To avoid curing caused by light exposure, these formulations were kept in a dark environment. The 3D printing process was made by using a Prusa SL1S SPEED printer, followed by a post-curing phase of 60 s under a DYMAX ECE Flood lamp, set to a light intensity of 130 mW/cm^2.

2.4. Characterization

2.4.1. Attenuated total reflectance fourier transform infrared spectroscopy (ATR-FTIR)

To monitor the photocuring process, a Nicolet iS 50 Spectrometer was employed, with data analysis conducted using OMNIC software provided by Thermo Fisher Scientific. For the reaction analysis, a stir bar was utilised to spread the viscous resin over a silicon support that had a thickness of 32 μm. The spectral resolution was set at 4 cm^{-1}. The conversion was assessed by monitoring the reduction in the area associated with the acrylate double bond, which is centred around 1620 cm^{-1}, while the peak at 2930 cm^{-1} was used as a reference. Equation 1 was applied to numerically evaluate the conversion during the irradiation with UV light.

$$Conversion\ (\%) = \frac{\left(\frac{A_{group}}{A_{ref}}\right)_{t=0} - \left(\frac{A_{group}}{A_{ref}}\right)_{t}}{\left(\frac{A_{group}}{A_{ref}}\right)_{t=0}} \times 100$$

Equation 1. Percentage of conversion calculated from FTIR analysis. A_{group} corresponds to the acrylate group area investigated, A_{ref} is the reference area at 2390 cm^{-1}

2.4.2. Photo dynamic scanning calorimetry (photo-DSC)

A photo-DSC was used to follow the advancement of the photocuring reaction. The configuration consisted of a Mettler TOLEDO DSC-1 integrated with a Gas Controller GC100 and a Hamamatsu LIGHTINGCURE LC8 mercury lamp (from Hamamatsu Photonics).

Table 2
Formulation AESO:IBOA with different types of bioactive glasses based on the silanization method.

AESO (%wt)	IBOA (%wt)	BGs (phr)	BGs type	Name
70	30	30	S4	AI
		30	Cu–S4	AI-Cu
		30	Silanised S4	AI-Sil 2h
		30	Silanised S4	AI-Sil 2h pH 5
		30	Silanised S4	AI-Sil 24h
		30	Silanised Cu–S4	AI-Cu-Sil 2h
		30	Silanised Cu–S4	AI-Cu-Sil pH 5
		30	Silanised Cu–S4	AI-Cu-Sil 24h
		0	–	AIref

The UV light had a 365 nm wavelength, with an intensity adjusted to 10 % of the maximum output, resulting in 10 mW/cm^2. An open aluminium pan contained 5–15 mg of resin, while an empty aluminium pan was utilised as a reference. 40 ml/min nitrogen flow was used to maintain an inert chamber at room temperature (25 °C).

The photo DSC procedure involved the sample settling for 2 min, followed by 10 min of UV light exposure, divided into two irradiation steps of 10 min each. The second irradiation was essential to establish the baseline, which was determined by subtracting the second curve from the first one. Mettler Toledo STARe software V9.2 was used to process the data.

2.4.3. Rheology and photo-rheology

Anton Paar MCR302 parallel plate rheometer was used to determine the viscosity through the rheology experiment and the behaviour in function of the irradiation through the photo-rheology. Photo-rheology tests were performed using a Hamamatsu LC8 UV lamp set to 30 mW/cm^2. The light was activated 1 min after the start of the test and adjusted to half of its maximum power, which corresponded to 15 mW/cm^2. A glass plate was used as the lower plate, allowing the radiation to pass through. The plate gap was set to 0.3 mm. A constant frequency of 1Hz was used to measure the experiments, and the temperature was set to 25 °C. Both storage and loss modulus (G′ and G″) were monitored during the tests. During deformation, G′ represents the elastic component of the material and G″ indicates the viscous component.

Additionally, rheological testing was performed to determine the viscosity formulations, and to determine their compatibility for the 3D printing process. For this analysis, two 25 mm diameter metallic plates were employed, maintaining a 1 mm gap between them. Viscosity measurements were measured over a 0.01 to 1000 s-1 shear rate range.

2.4.4. Contact angle

Pressed BGs were used to determine the hydrophilicity of the samples. An ultrapure water droplet was placed on the surface and the contact angle measurement was determined. The analysis was repeated in triplicate and performed by a Drop SHApe Analyzer, DSA100, Krüss.

2.4.5. 3D printing process

3D printing was performed using a commercial Masked Stereolithography Apparatus (MSLA) printer, specifically the SL1S SPEED model from Prusa, Czech Republic. The printer light source corresponds to a monochromatic LED source of 405 nm with 25 W of power. After printing, the object underwent a post-curing process in a DYMAX lamp for 60 s to complete the photopolymerization. The biobased resin, which is light-sensitive at 405 nm, was cured layer by layer, each with a 50 μm thickness, for 5 s per layer. After printing, the samples were cleaned with isopropanol to eliminate any uncured resin remaining on the surface. A final curing step was performed for 30 min under a 405 nm Phrozen Cure Lamp.

2.4.6. Dynamic mechanical thermal analysis (DMTA)

Dynamic Mechanical Thermal Analysis (DMTA) of the 3D-printed materials was performed using a Triton Technology instrument. The temperature range for the analysis was selected from 0 °C to 100 °C, with a heating rate set at 5 °C per minute. The test applied uniaxial tensile stress at a frequency of 1 Hz, to identify the glass transition temperature (T_g), which corresponds to the peak of the tan δ curve. The highest test temperature was chosen based on the material's rubbery plateau phase. The samples tested, measuring 1.5 × 3.5 × 12 mm, were produced via 3D printing using the Prusa SL1S SPEED as described in section 2.4.5. The crosslink density (ν_c) was determined using Equation 2.

$$\nu_c = \frac{E'}{3RT}$$

Equation 2. Formula used to determine the number of crosslinks per volume (ν_c).Where E′ corresponds to the storage modulus in the rubbery plateau (T_g+50 °C), T is the temperature where E' is taken in Kelvin and R is the gas constant.

2.4.7. Tensile test

Mechanical properties of the 3D-printed materials were evaluated through stress-strain tests using an MTS QTest™/10 Elite testing machine equipped with a 500 N load cell. The machine was set to a crosshead speed of 5 mm/min. Young's modulus (E) was derived from the slope of the linear portion of the stress-strain curve, while the stress and strain at break were measured at the point where the samples failed. The results presented are the average values obtained from five dog-bone-shaped samples, which were printed according to the ISO-527A Type 5B standard.

2.4.8. Composite scaffolds characterization

The composite 3D printed scaffolds were fully characterized, focusing on the morphology, composition, in vitro reactivity in simulated body fluid (SBF) according to Kokubo's protocol [81], cytocompatibility and metabolic activity. All the analysis will be described in the following paragraphs. To analyse the scaffolds fracture surface, field emission scanning electron microscopy (FESEM) with energy dispersive X-ray spectroscopy (EDS) capabilities (SUPRA™ 40, Zeiss, Oberkochen, Germany) was employed, along with X-ray diffraction (XRD) analysis (Malvern PANalytical X'Pert PRO diffractometer) to examine their morphological and compositional properties. Specimen preparation involved breaking either 3D printed DMTA or 3D printed tensile samples through the brittle fracture, then mounting them on aluminium stubs with a silver-based adhesive, followed by platinum (Pt) metallization for analysis.

2.4.9. Simulated body fluid (SBF)

In vitro reactivity in simulated body fluid (SBF) was evaluated by immersing the filled scaffolds in the prepared solution, following the Kokubo protocol [82]. The samples were kept in an orbital shaker at 37 °C and 120 rpm for 28 days; then their surface was evaluated at different periods to determine the hydroxyapatite formation employing EDS, SEM images and XRD analysis.

2.4.10. In vitro cytocompatibility assessment

2.4.10.1. Cells cultivation. Before conducting biological assays, the samples were sterilized by exposure to UV-C light for 30 min on each side. Human bone marrow-derived mesenchymal stem cells (hbMSCs) were obtained from Promo-Cell (C-12974) and grown in low-glucose Dulbecco's modified eagle medium (DMEM; Sigma-Aldrich, Milan, Italy), which was supplemented with 10 % fetal bovine serum (FBS; Sigma-Aldrich, Milan, Italy) and 1 % antibiotics. The cells were incubated at 37 °C in an atmosphere of 5 % CO_2 until they reached 80–90 % confluence. They were then detached using a 0.25 % solution of trypsin-EDTA in phosphate-buffered saline (PBS), collected, and prepared for experimentation.

2.4.10.2. Cytocompatibility evaluation. Cells were seeded directly onto the surface of the specimens (A7I3-ref, A7I3–S4, A7I3–S4-sil, A7I3–Cu, and A7I3–Cu-sil) at a desired density of 2×10^4 cells per sample. After a 4-h incubation period to facilitate adhesion, 700 μL of DMEM was added to each specimen, and the cells were cultured for 24 h. Cell viability was determined at various times using the resazurin-based alamarBlue™ assay (ready-to-use solution; Life Technologies, Milan, Italy) to measure metabolic activity. According to the manufacturer's instructions, alamar blue reagent at concentration of 0.015 % in PBS,was applied to the seeded samples, and after 4 h of incubation in darkness, relative fluorescent units (RFU) were measured using a spectrophotometer (Spark, Tecan, Switzerland).

Surface-attached cell morphology was examined using scanning electron microscopy (SEM; JSM-IT500, JEOL, Japan). Samples were dehydrated with an ascending gradient of ethanol (70–90 % ethanol for 1 h each and 100 % ethanol for 2 h), fast-dried with hexamethyldisilazane, mounted on stubs using conductive carbon tape. Images were taken at varying magnifications after coating them with a thin gold layer (JEOL smart coater, JEOL, Japan).

2.4.11. In vitro antibacterial assessment

2.4.11.1. Growth culture medium. The antibacterial activity of the specimens was tested against multi-drug resistant *Staphylococcus aureus* (MDR *S. aureus*), a Gram-positive bacterium obtained from the American Type Culture Collection (ATCC 43300). This strain, recognized for its resistance to multiple antibiotics, is a standard model for testing the antibacterial efficacy of materials and is a major cause of bone infections [83]. The bacteria were cultured on Luria-Bertani agar (LB, Sigma-Aldrich, Milan, Italy) and incubated at 37 °C until single and countable colonies appeared. The following day, a fresh bacterial suspension was prepared as explained in previous article to a final concentration of 1×10^5 CFU/mL [82].

2.4.11.2. In vitro antibacterial activity assessment. The antibacterial properties of the specimens (A7I3-ref, A7I3–S4, A7I3–S4-sil, A7I3–Cu, and A7I3–Cu-sil) were evaluated according to the International Organization for Standardization protocol (ISO 22196). Sterile samples were placed in a 24-well plate, and 100 μL of a bacterial suspension with the desired cell count was applied directly onto their surfaces, with the A7I3-ref sample serving as the control. After 24 h of incubation at 37 °C, non-adherent bacteria were removed by washing with PBS, and the metabolic activity of the surface-adhered bacteria was measured using the resazurin-based alamar Blue assay (0.0015 % in PBS; described in section 2.4.10.2).

The number of viable bacteria adhering to the surfaces was determined using the colony-forming unit (CFU) method. Bacteria were mechanically detached from the surfaces by sonication and vortexing. Viable colonies were then counted following to the previous article [82].

Additionally, the morphology of bacteria adhered to the surfaces and the formation of bacterial aggregates was analyzed using scanning electron microscopy (SEM) as detailed in section 2.4.10.2.

Two software programs were employed to assess the thickness, distribution of bacterial colonies, and the surface area occupied by the bacteria: SMILE VIEW™ map (version 8.2.9621, JEOL) and ImageJ. High-magnification SEM images (× 5000) were processed by removing background noise through threshold adjustments. SMILE VIEW software was used to determine the 3D image of the bacteria, providing data on their thickness, height, and distribution, represented as peaks. In ImageJ, bacterial cells were automatically counted, and the surface area occupied by the bacteria on the specimens was calculated.

2.5. Statistical analysis

All experiments were conducted in triplicate, and the results were analyzed statistically using SPSS software (version 20.0, IBM). The Shapiro–Wilk test was used to verify the normal distribution of the data, and Levene's test confirmed the homogeneity of variance. Comparisons between groups were performed using a one-way ANOVA, followed by Tukey's post hoc test for further analysis. Differences were considered statistically significant when p-values <0.05.

3. Results and discussion

3.1. Bioactive glass silanization

After activating the bioactive glasses using acetone, as described in section 2.2.1, both S4 and Cu-doped glasses were immersed in a solution of 20 % TMSPMA in ethanol.

Nguyen et al. have demonstrated that silanization, particularly using TMSPMA, is an efficient approach to improve the dispersion of particles within a polymeric matrix, reducing their natural tendency to aggregate. The dispersion enhancement significantly increases the mechanical properties of the composite materials [84,85]. TMSPA is a practical choice due to its protocol as a silanizing agent; in fact, it avoids hazardous solvents like xylene and utilizes ethanol as a safer and environmentally friendly solvent.

Chemically, the silanization process consists of a hydrolysis and condensation reaction of the trimethoxysilane groups in TMSPMA. Upon hydrolysis, the methoxy (-OCH_3) groups are converted into silanol (-SiOH) groups in the presence of water. These silanol groups react in turn by condensation with hydroxyl groups present on the glass surface, allowing the forming of solid Si–*O*–Si bonds. This covalent linkage attaches the TMSPMA molecules to the particle surface, providing a stable interface.

Furthermore, the remaining methacrylate groups (-CH_2═C(CH_3)–COO-) in TMSPMA also participate in the chemical integration of the silanization agent to the matrix. These groups can participate in the photocuring reactions, forming covalent bonds with the polymer network. This double functionality ensures a better distribution and dispersion of the bioactive glass particles within the polymeric matrix, making the TMSPMA a perfect candidate for this silanization process.

To graft TMSPMAon the bioactive glass surface, three different silanization methods were tested: i) mixing the glass powder with a magnetic stirrer for 2 h; ii) 2-h mixing plus keeping the pH of the solution at 5 using acetic acid; iii) mixing the solution for 24 h. After the process, the samples were characterized by ATR FTIR and contact angle to determine the effect of the silanization.

The ATR-FTIR analysis, shown in Fig. 1a and b, compares the untreated glass samples, the silanization agent, and the treated glasses. The analysis revealed that all functional groups belonging to TMSPM were present in the treated samples, indicating a successful surface functionalization of the bioactive glasses. Since the FTIR is a qualitative analysis, it was determined that all the methods were efficient in functionalizing the BGs.

Similar to FTIR analysis, contact angle measurements confirmed the surface modifications of the glasses after silanization. A drop of ultrapure water was deposited onto the pre-pressed BG surface, and the resulting contact angle measurements are reported in Fig. 2. The images confirmed that all silanized glasses exhibited increased hydrophobicity, indicating the successful attachment of aliphatic chains to the glass surface. In contrast, the non-silanized glass remained completely hydrophilic, instantly adsorbing the water drop.

When comparing the contact angles across different methods, it is noticeable that the Cu-silanized glass did not show significant changes between the process methods, suggesting consistent hydrophobicity regardless of the chosen process. However, the differences were more evident in the case of S4 glass. The 2 h method at pH5 and the 24-h method produced comparable results, whereas the 2 h method led to a less hydrophobic surface.

Based on these observations, the 2-h silanization at pH5 and 24-h silanization methods were selected as the most efficient for both types of BGs. Ultimately, the 24-h method was chosen due to its consistency with the project's emphasis on using low-impact reagents and sustainable processes, as it requires fewer additional compounds, such as acetic acid, to adjust the pH.

For the Cu-doped glasses, however, the 24-h silanization method posed a potential issue. During 24 h of immersion, the Cu ions could dissolve into the solution, causing the unintended removal of Cu doping from the glass. To address this concern, we performed an EDS analysis on the BGs after the silanization process. The Cu weight percentage was calculated, resulting in 4.1 wt% for both the 2-h and the 2-h at pH 5 methods, while the 24-h method yielded 3.9 wt%. The consistency in the Cu percentage clearly shows that the 24-h process does not result in significant copper ions leaching from the glass particles.

Given these findings, all BGs incorporated into the resin will be considered silanized using the chosen 24-h treatment method.

3.2. Photo curing process

The photocurable and biobased resin behaviour under UV light with different types of BGs was investigated using three different methods: transmission FTIR, photo-DSC, and photorheology. The BGs content in all the UV-curable formulations was maintained at 30 phr, based on our

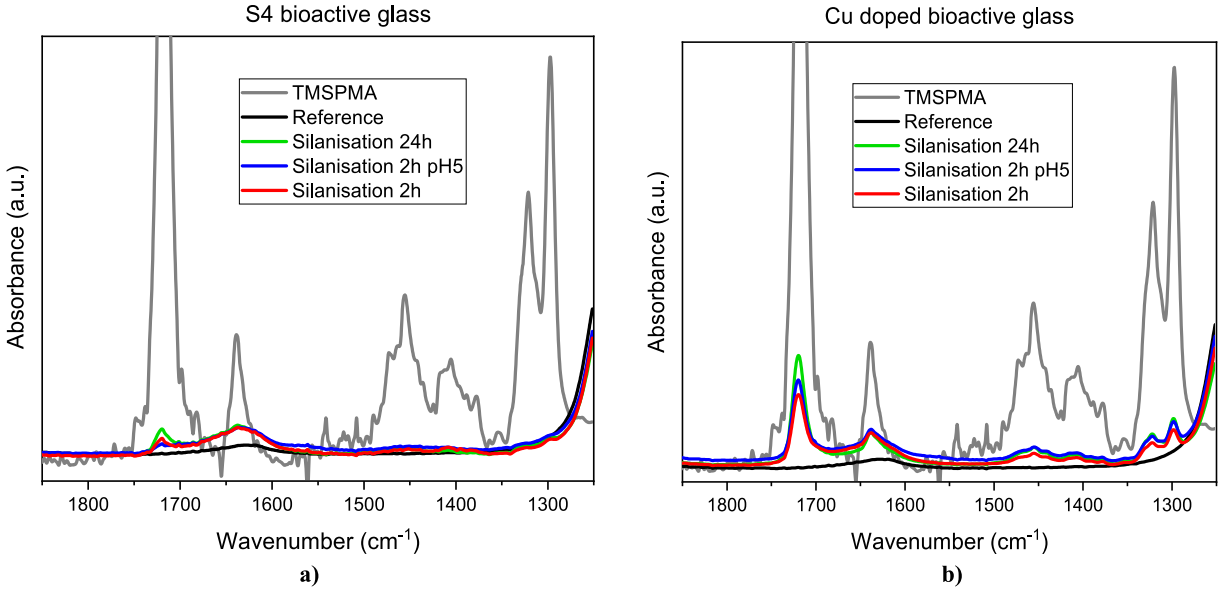


Fig. 1. FTIR spectra of **a)** silanized S4 BGs compared with the reference (composition with not silanized BGs) and TMSPMA and **b)** silanized S4 Cu doped BGs compared with the reference (composition with not silanized Cu-BGs) and TMSPMA.

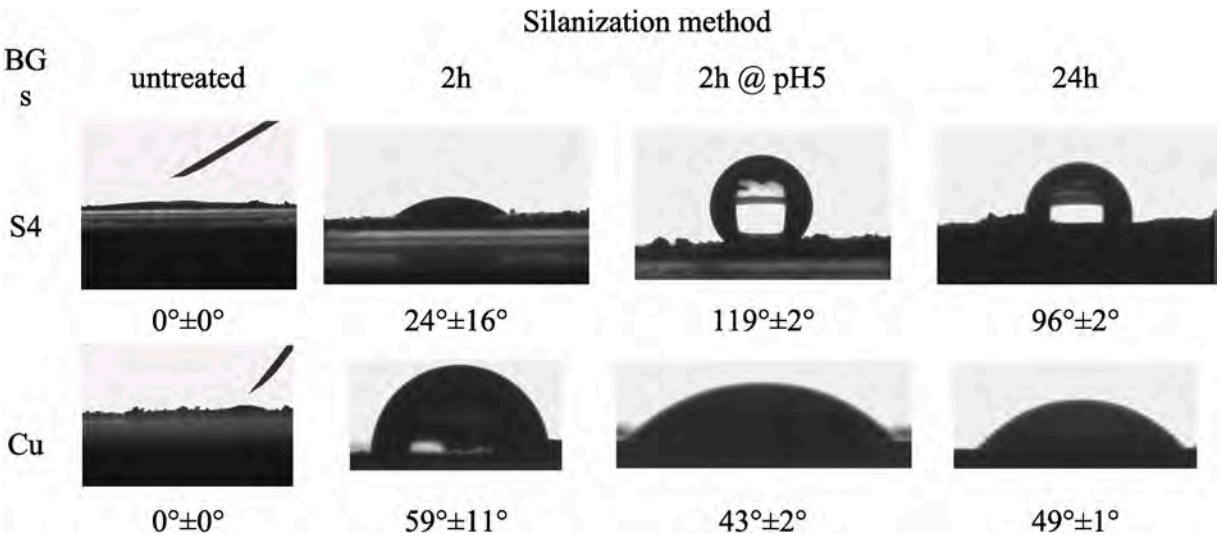


Fig. 2. Different images and relatives' numeric values corresponding to the contact angle of a drop of ultrapure water deposited onto the surface of BGs treated differently.

previous investigations [86].

3.2.1. Attenuated total reflectance fourier transform infrared spectroscopy (ATR-FTIR)

Transmission FTIR evaluated the acrylate double bond conversion upon UV irradiation by monitoring the peak decrease centred around 1620 cm^{-1}. Representative curves obtained from transmission FTIR recorded during UV-light irradiation are shown in Fig. 3b. The reported curve represents typical behaviour observed across all formulations. The conversion curves for all the formulations tested are presented in Fig. 3a, with the conversion data summarized in Table 3.

As expected, the results reported in Fig. 3 and summarized in Table 4 indicate that the presence of BGs decreases the final conversion of the acrylate double bond, while the slope of the conversion curves remains comparable across formulations as a function of irradiation time. This outcome was expected, as glass fillers can influence light penetration during irradiation and even compete with the photoinitiator for light absorption. The BGs influence is likely due to the inert nature of the glass, which leads to competitive absorption of light between the glass particles and the photoinitiator, thereby reducing the generation of photoinduced reactive initiating species. Furthermore, the silanized BGs lead to an additional decrease in the final double bond conversion upon irradiation, although these values remain within an acceptable range for complete curing process.

Table 3
Final conversion of the photocurable polymeric matrix after 120 s UV-light irradiation obtained by following the decrease of the acrylate peak by means of FTIR.

Sample	Conversion (%) after 120s irradiation
A7I3-ref	86 ± 2
A7I3–S4	73 ± 2
A7I3–S4-sil	54 ± 5
A7I3–Cu	68 ± 2
A7I3–Cu-sil	57 ± 1

3.2.2. Photo dynamic scanning calorimetry (photo-DSC)

Photo-DSC was used to validate the ATR-FTIR analysis. The

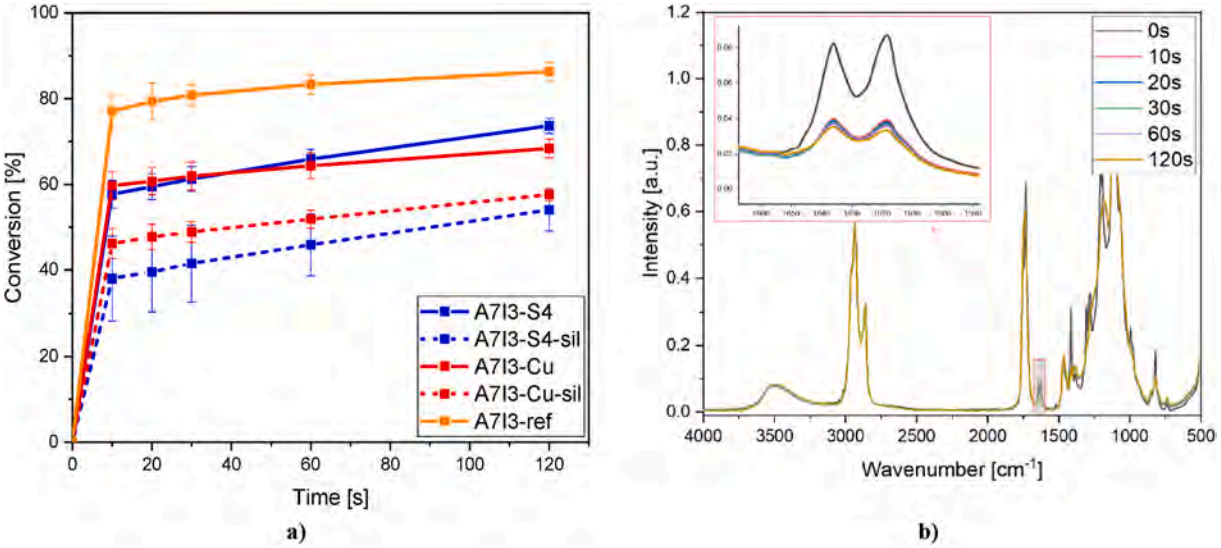


Fig. 3. a) Conversion curves as a function of irradiation time for the formulation A7I3 (from ATR-FTIR) as a function of time varying the different bio-glass at 30 phr content. Light intensity was set at 130 W/cm^2 **b)** Representative FTIR graph reproduced in all the formulations and magnification of the acrylate peak decrease.

Table 4
Heat released by the photocuring reaction measured during photo-DSC analysis with different types of bioactive glasses.

Sample	Integral [J/g]
A7I3-ref	256 ± 33
A7I3–S4	215 ± 16
A7I3–S4-sil	144 ± 25
A7I3–Cu	203 ± 10
A7I3–Cu-sil	156 ± 5

exothermicity data for all the formulations taken in consideration is reported in Table 4 and Fig. 4.

The data reported are consistent with the FTIR analysis. The photo-DSC results show that incorporating bioactive glass slightly reduces the heat released during UV curing, which aligns with the observed decrease in acrylate double bond conversion measured by FTIR. As previously noted, the silanized fillers further reduced the overall heat release due to lower double bond conversion.

3.2.3. Rheology and photo-rheology

The formulation was also subjected to photo-rheology analysis to determine the optimal conditions for a 3D printing process and confirm the success of the curing process. The rheological curves obtained upon UV irradiation, shown in Fig. 5a, indicate that all the analyzed formulations simultaneously reached a constant G' modulus. This suggests that the silanization process does not affect the kinetics of the curing process. Additionally, the gelation time remained consistent at approximately 5 s, regardless of the composition. These findings provide further evidence about the optimal curing process.

Based on all the experiments conducted on the photo-curable formulations, it can be confirmed that they are highly responsive to UV light, allowing the photocuring process to be activated without any delay. Notably, the silanization of bioactive glasses does not significantly hinder the photocuring process, ensuring efficient curing across all formulations.

Rheological tests were performed to investigate the viscosity of the photo-curable formulations and their compatibility with the 3D printing process. The viscosity curves as a function of the applied shear rate are presented in Fig. 5b, with all relevant data summarized in Table 5.

Table 5 shows that the viscosity values obtained for all the formulations closely match the theoretical viscosity required for a 3D printing process, which needs to be less than 5 Pa*s at 30s^{-1} according to the literature [87–94]. All the formulations meet the criteria for a successful 3D printing process.

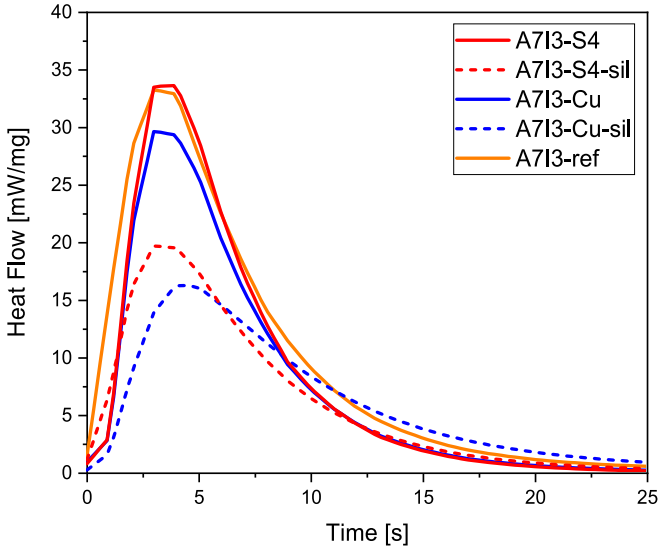


Fig. 4. Heat released by the photocuring reaction during UV-light irradiation of A7I3 formulation as a function of time.

3.3. The 3D printing process

All the previously characterized formulations were 3D printed using a Prusa SL1S printer.

The DLP method was specifically chosen because it enables high precision, smooth surfaces, and uniform distribution of bioactive glass within the polymer matrix. It also supports the efficient manufacturing of designs with controlled porosity, which is particularly beneficial for applications requiring bioactivity and cellular interaction.

Various shapes were printed, including samples for dynamic thermal analysis (DMTA), dog bone shape samples for tensile tests, and squared samples for compression tests. As shown in Fig. 6, complex and hollow shapes were also successfully printed, demonstrating the effectiveness of the 3D printing process. This confirms that, as achieved in previous studies, it is possible to easily create complex structures tailored in shape and porosity.

3.4. Characterization of 3D-printed scaffolds

3.4.1. SEM analysis

Scanning Electron Microscope (SEM) analysis was conducted on the fracture surface of the 3D-printed samples. Fig. 7a and b presents SEM images of the S4-reinforced samples, both with silanized and pristine glass, while Fig. 7c and d shows the samples containing Cu-doped bioactive glasses. The images reveal that all the samples exhibit well-dispersed BGs particles throughout the biobased polymer matrix.

A closer examination of the composites containing silanized glasses compared to the non-salinized counterparts reveals a significant improvement in the interface between the reinforcement and the polymeric matrix. When non-silanized glasses are used, voids can be observed at the interface during brittle fracture, caused by the detachment of the reinforcement, indicating poor glass-polymer matrix interaction and a week interface.

In contrast, as also evidenced by other authors [95] when silanized glasses are employed, no noticeable voids between glass particles and matrix are observed, suggesting a stronger interface. This indicates that the fracture occurs within the polymer matrix rather than at the matrix-glass interface.

Additionally, the SEM images of the samples containing silanized glasses appear less clear compared to those with non-silanized glasses. This reduced definition is attributed to the silanization process, which causes a strong bond with the polymer matrix. The interface between the particles and polymer matrix is strong and continuous; therefore, the fracture does not occur at the interface but within the polymer matrix. The glass particles are coated with a layer of polymeric matrix, and since the matrix is less conductive than the BGs, the SEM images, which rely on electron conduction, are less defined.

By analysing the BGs particles embedded in the matrix, their mean diameters were determined. As reported in our previous study [50], the S4 particles had a mean diameter of 482 ± 59 nm. In contrast, the Cu-doped particles displayed a slightly reduced mean diameter of 412 ± 67.

3.4.2. Dynamic mechanical thermal analysis (DMTA)

DMTA was used to assess the viscoelastic properties of the photo-cured AESO-based materials. The collected data are presented in Fig. 8 and Table 6. The analysis reveals minimal difference in the glass transition temperature (T_g) between scaffolds containing silanized and non-silanized S4 BGs. However, a slight decrease in T_g is observed in the samples containing Cu-doped BGs.

The incorporation of Cu-doped bioactive glass could cause a slight reduction in the final T_g compared to the non-doped formulation,

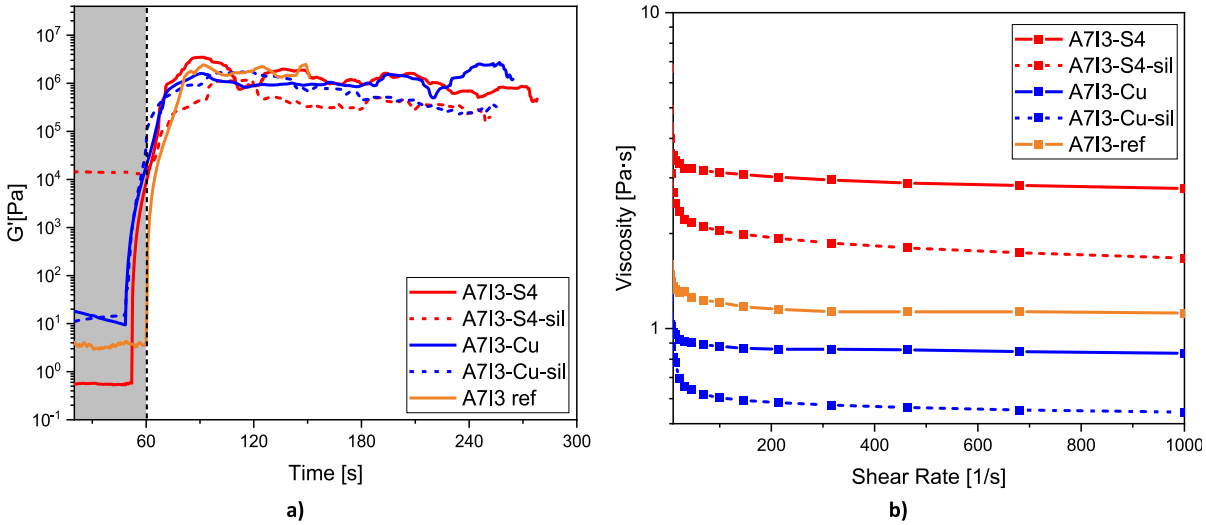


Fig. 5. a) Photo-rheology results of all formulations. UV-light irradiation started after 60 s. **b)** Rheology curves obtained for all the biobased formulations reinforced with BGs.

Table 5
Viscosity value measured at 30 s^{-1} measured with a parallel plate of 2.5 mm diameter.

Sample	Viscosity [Pa*s] at 30s^{-1}
A7I3-ref	1.1
A7I3–S4	4.0
A7I3–S4-sil	2.6
A7I3–Cu	0.8
A7I3–Cu-sil	0.6

possibly due to the competitive light absorption effect of the Cu element. Cu, which imparts a blue colour to the material, absorbs more UV light than a white-coloured material, potentially interfering with the cross-linking process during UV exposure. This is supported by the lower percentage of conversion, as evaluated by FTIR analysis and confirmed by photo-DSC values.

3.4.3. Tensile tests

Tensile tests on the 3D-printed, composite scaffolds were used to determine the impact of the BG silanization process on their mechanical properties. The tests measured the elastic modulus, elongation at break, and stress at break. All the collected data are presented in Fig. 9 and summarized in Table 7.

The filled scaffolds exhibited an overall enhancement in mechanical performance. Furthermore, silanization significantly enhances the mechanical properties across all the measurements. Specifically, the elastic modulus increased by an impressive 70 % for the S4 samples and by 40 % for the Cu-reinforced samples. Additionally, the stress at break improved by 35 % for both S4 and Cu-reinforced samples, while the strain at break remained almost unchanged.

This improvement highlights the effectiveness of the silanization process, evidencing the pivotal role of silane as a linker between the polymeric matrix and the glass particles. The aliphatic chains attached to the surface of the BGs suggest the formation of a strong interface with the polymer matrix, yielding outstanding enhancements in terms of mechanical properties.

3.4.4. Simulated body fluid (SBF) immersion

After immersing the Cu-doped samples in SBF for 28 days at 37 °C, their surfaces were analyzed using FESEM and XRD analyses. The A7I3–Cu samples were selected as the reference for this analysis, as Cu doping typically presents the most challenging conditions for hydroxyapatite (HAp) growth due to Cu's potential to hinder HAp formation.

FESEM images of the scaffold surface on both the 7th and 28th days are shown in Fig. 10. On the 7th day, initial HAp crystals are visible, and by the 28th day, the well-formed HAp lamellae are evident. To confirm the formation and presence of HAp, an EDS analysis was conducted, and the Ca/P ratio was determined to be 1.65, closely matching the theoretical ratio of 1.67, thus verifying HAp presence [96].

Final confirmation was obtained through XRD analysis, where all theoretical peaks corresponding to HAp are represented in Fig. 10d [97].

Then, the obtained results show that the copper present in the bioactive glass does not hinder the bioactivity of the material, as observed by other authors for other glass compositions [98–100]. Furthermore, the silanization allows an excellent dispersion and exposure of the glass on the surface of the samples, thus permitting the mechanisms activation of the bioactivity process. These findings conclusively demonstrate that the samples successfully supported the growth of hydroxyapatite, confirming their bioactivity and potential for bone regeneration applications.

3.5. In vitro cytocompatibility evaluation

After confirming the success of silanization and doping the samples with Cu and evaluating the characterization of the samples' surfaces, the study moved on to assess the surface impacts on the attachment and spread of the hbMSCs. hbMSC with their intrinsic differentiation potential into bone cells, are suitable candidates for this application [101]. The metabolic activity and morphology of the surface-attached cells were evaluated using alamar blue assay (which results are shown here as RFU values as detailed in section 2.4.10.2) and SEM images after 24 h of direct contact with the samples' surfaces. The results are presented in Fig. 11. A7I3-ref is considered the control sample, and the obtained results were compared to it.

As shown in Fig. 11a, the metabolic activity of the cells attached to the surfaces of A7I3–S4 and A7I3–Cu was similar to that of the control sample (A7I3-ref) with no significant differences ($p > 0.05$). However, the cells attached to the surfaces treated with silanization demonstrated statistically significantly lower metabolic activity than the control sample ($p < 0.01$, indicated by **). This reduction could be explainable by either a small number of attached cells or a decrease in the cells' metabolic rate. SEM images showed well-spread cells on the surfaces of A7I3-ref (control), A7I3–S4, and A7I3–Cu. In contrast, on the A7I3–S4-sil surface, some non-attached cells were observed (red arrow);

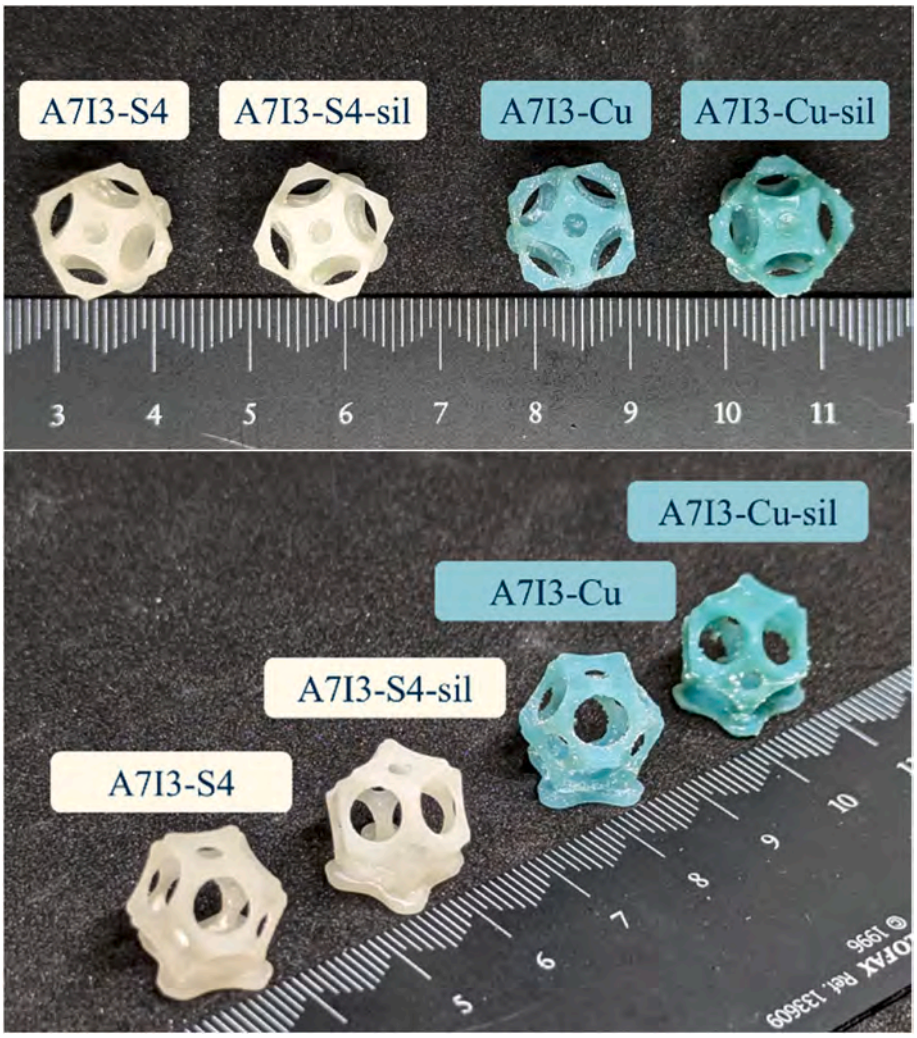


Fig. 6. 3D printed biobased BGs reinforced scaffolds from different points of view.

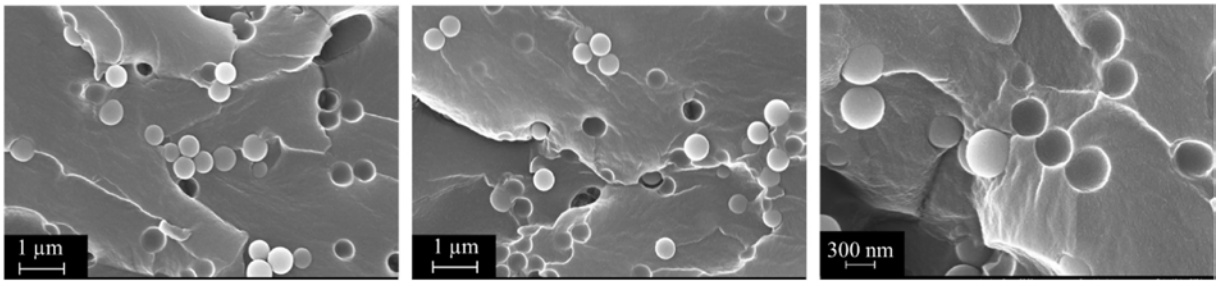


Fig. 7a. A7I3–S4 sample surface fracture.

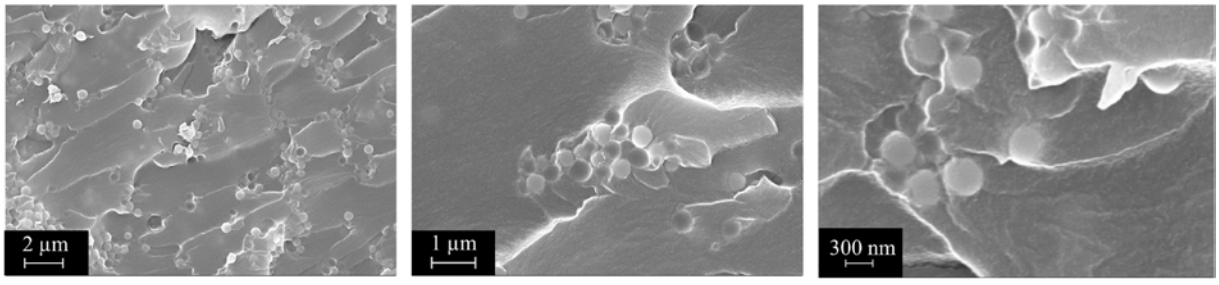


Fig. 7b. A7I3–S4-sil sample surface fracture.

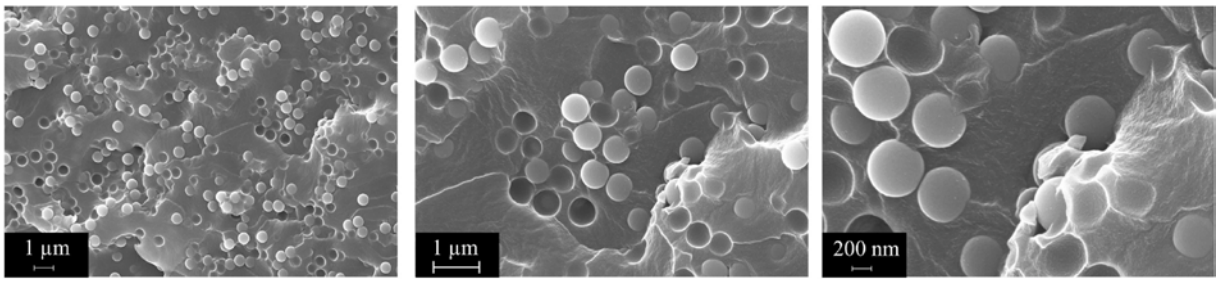


Fig. 7c. A7I3–Cu sample surface fracture.

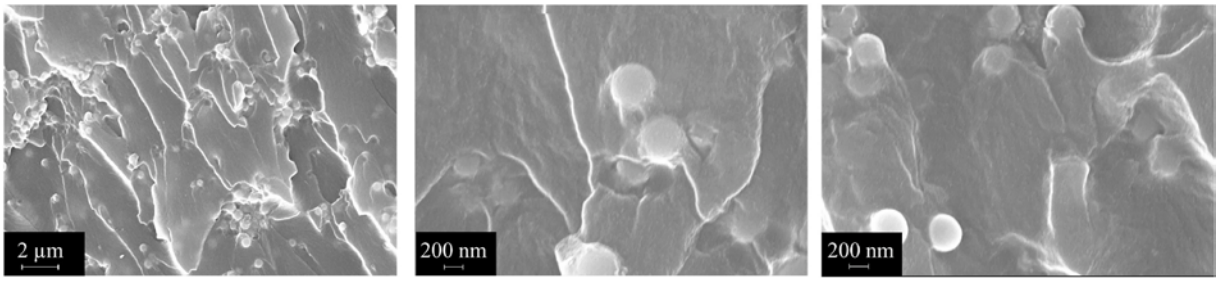


Fig. 7d. A7I3–Cu-sil sample surface fracture.

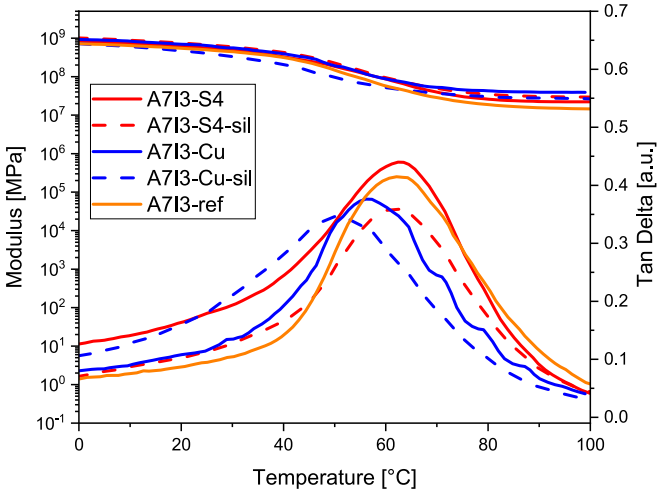


Fig. 8. Tan Delta and elastic modulus curves obtained by DMTA analysis.

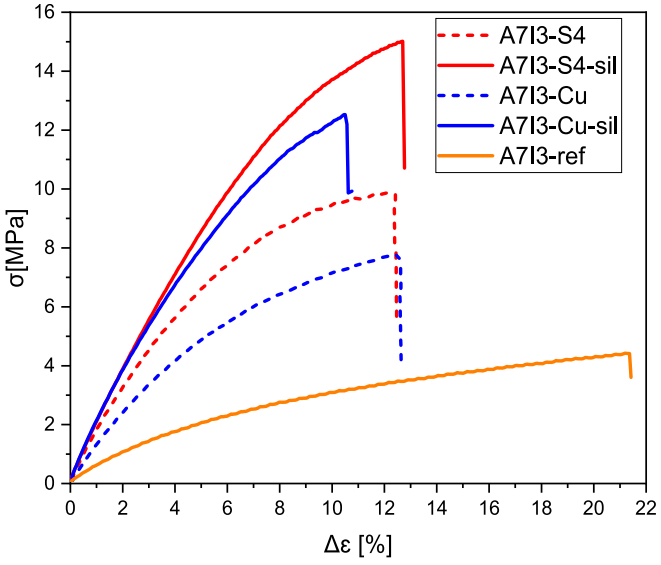


Fig. 9. Stress-strain curves obtained from tensile tests.

Table 6
Results obtained by DMTA analysis for samples variable bio-glasses and IBOA rates. T_g was calculated as the maximum of tan δ. ν_c calculated by Equation 2.

Sample	Glass transition temperature T_g [°C]
A7I3-ref	60 ± 0
A7I3–S4	61 ± 2
A7I3–S4-sil	60 ± 2
A7I3–Cu	56 ± 0
A7I3–Cu-sil	50 ± 1

Table 7
Compressive modulus obtained from compression test.

Sample	Elastic modulus [MPa]	Stress at break [MPa]	Strain at break [%]
A7I3-ref	0.49 ± 0.15	4.86 ± 0.82	28.37 ± 5.28
A7I3–S4	0.59 ± 0.04	9.93 ± 0.61	12.55 ± 0.36
A7I3–S4-sil	1.87 ± 0.08	15.25 ± 0.41	13.22 ± 0.59
A7I3–Cu	1.17 ± 0.21	8.20 ± 2.49	14.88 ± 3.56
A7I3–Cu-sil	1.85 ± 0.15	12.86 ± 1.84	11.07 ± 0.74

additionally, the attached cells (highlighted by the yellow arrow in Fig. 11b) did not exhibit the typical morphology of the hbMSCs.

This finding aligns with the hydrophilicity analysis performed using contact angle measurements, which demonstrated that after silanization, the hydrophobicity of A7I3–S4-sil increased from 0° ± 0° (untreated sample) to 96° ± 2°, categorizing it as a hydrophobic surface [102]. This increase in hydrophobicity can mitigate cell attachment to the surfaces, as evidenced in the SEM images, and could contribute to the observed decrease in metabolic activity. SEM images of cells on the surface of A7I3–Cu-sil showed well-spread cells, but according to the

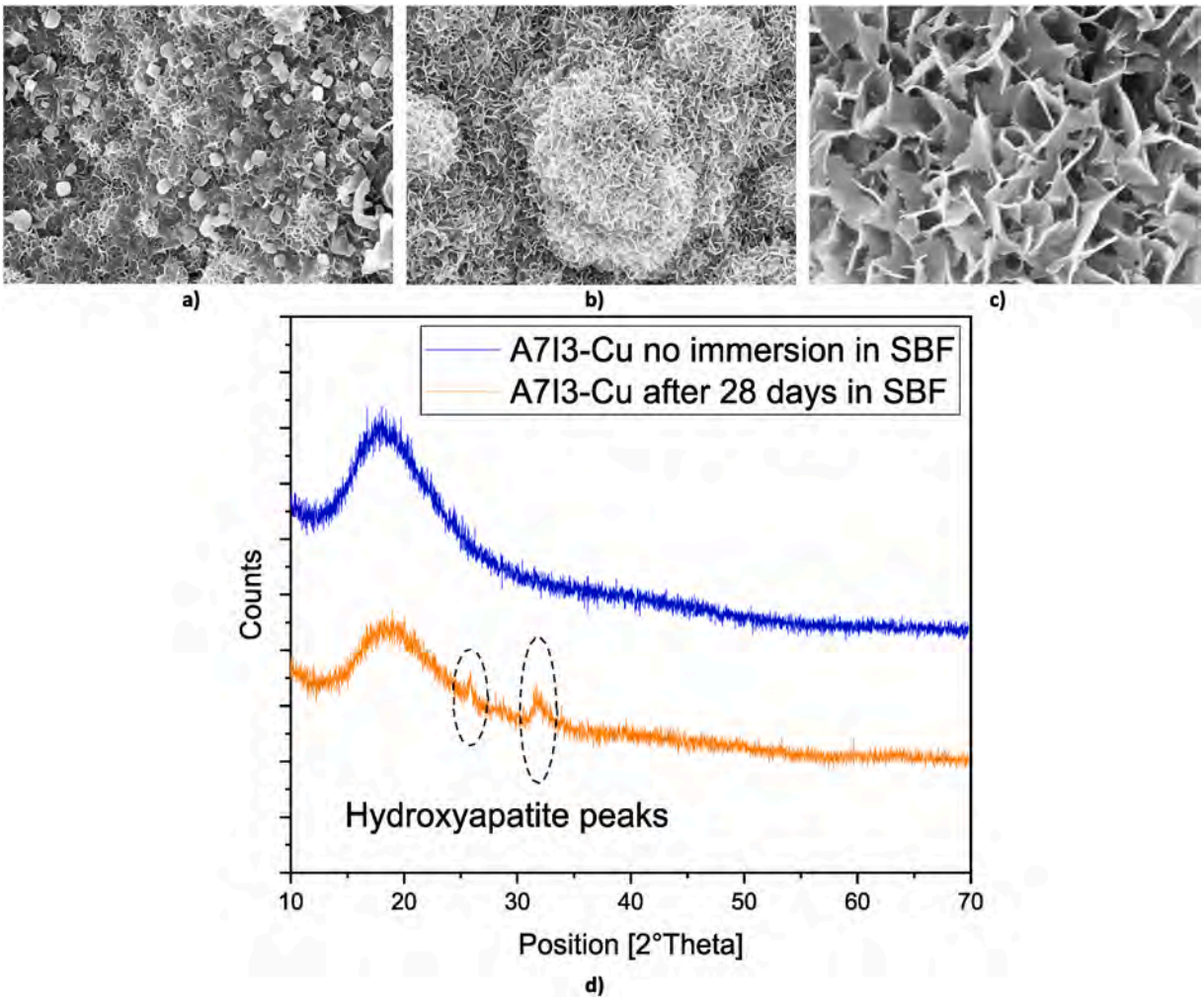


Fig. 10. Image of **a)** Crystal of HAp formed after 7 days, **b)** crystallized structure of HAp formed after 28 days, **c)** magnification of crystallized structure of HAp formed after 28 days. **d)** XRD of a A7I3–Cu sample not immersed in SBF (reference) and another sample immersed in SBF for 28 days. It is evident that the sample immersed in SBF for 28 days (orange line) contains the HAp peaks, evidenced with dotted ovals in the graph.

resazurine-based alamar blue assay, their metabolic activities were low. The results obtained from contact angle measurements did not show significant differences in the wettability of the surfaces, and even after silanization, the contact angle measurements remained within the hydrophilic category.

3.6. *In vitro antibacterial evaluation*

To evaluate the impact of the samples with binary modifications, doping with Cu and silanization, against bacterial pathogens, MRSA *S. aureus* was chosen as a representative of Gram-positive pathogens that can cause bone infections. According to the ISO 22196 protocol, the bacteria were directly infected on the sample surfaces and incubated for 24 h at 37 °C. Similar to previous experiments, A7I3-ref was considered the control sample, and the obtained results were compared with it. After the incubation period, the metabolic activity, viability, and morphology of the bacterial cells and aggregations were analyzed using the resazurin-based alamar blue assay, CFU, and SEM images (as explained in section 2.4.11.2). The results are presented in Fig. 12. The metabolic activity of the surface-adhered bacterial cells showed statistically significant differences between A7I3-ref (control) and A7I3–S4-sil, as well as between A7I3–S4 and A7I3–S4-sil, A7I3–Cu-sil ($p < 0.05$ indicated by *, Fig. 12a). Additionally, bacterial cells adhered to the surface of A7I3–Cu demonstrated a reduction in metabolic activity compared to A7I3-ref and A7I3–S4, although the difference was not statistically significant ($p > 0.05$, Fig. 12a). As shown in Fig. 12b, the number of viable bacterial cells adhered to the surface of A7I3-sil, A7I3–Cu, and A7I3–Cu-sil was approximately 57 % less than those on the surfaces of the control sample and A7I3–S4. Additionally, visualization of bacterial cells by SEM (Fig. 12c) and analyses performed on the 3D-reconstructed SEM images using two software programs, SMILE VIEW™ (MAP8.2.9621) and ImageJ (Fig. 13a and b), are explained in Section of 2.4.11.2, demonstrated that bacterial aggregations on the surfaces of A7I3-ref and A7I3–S4 occupied 13 % and 13.7 %, respectively, of the total surface area, with a maximum height (Z-maximum) of approximately 4.5 μm. This corresponds to 3–4 layers of bacteria, considering the dimension of *S. aureus,* which range between 0.5 and 1.5 μm. In contrast, on the samples treated with Cu-doping, silanization, and binary combination, sporadic and single bacterial cells were observed on their surfaces and the occupied surface area decreased from 13-14 % to 8–9%, with Z-maximum of approximately 2.5 μm. The eradication of the biofilm layer and having single bacterial colonies in medical device applications can be promising due to the increased sensitivity of single bacterial cells to even slight antimicrobial agents.

As expected from the previous analyses (mentioned above), the surface characteristics of A7I3–S4-sil shifted to hydrophobic after silanization, with a contact angle measurement of 94° ± 2°. The low metabolic activity and reduced bacterial adhesion on the surfaces of A7I3–Cu and A7I3–Cu-sil can be attributed to the presence of Cu ions on the sample surfaces. When bacterial cells irreversibly attach to the

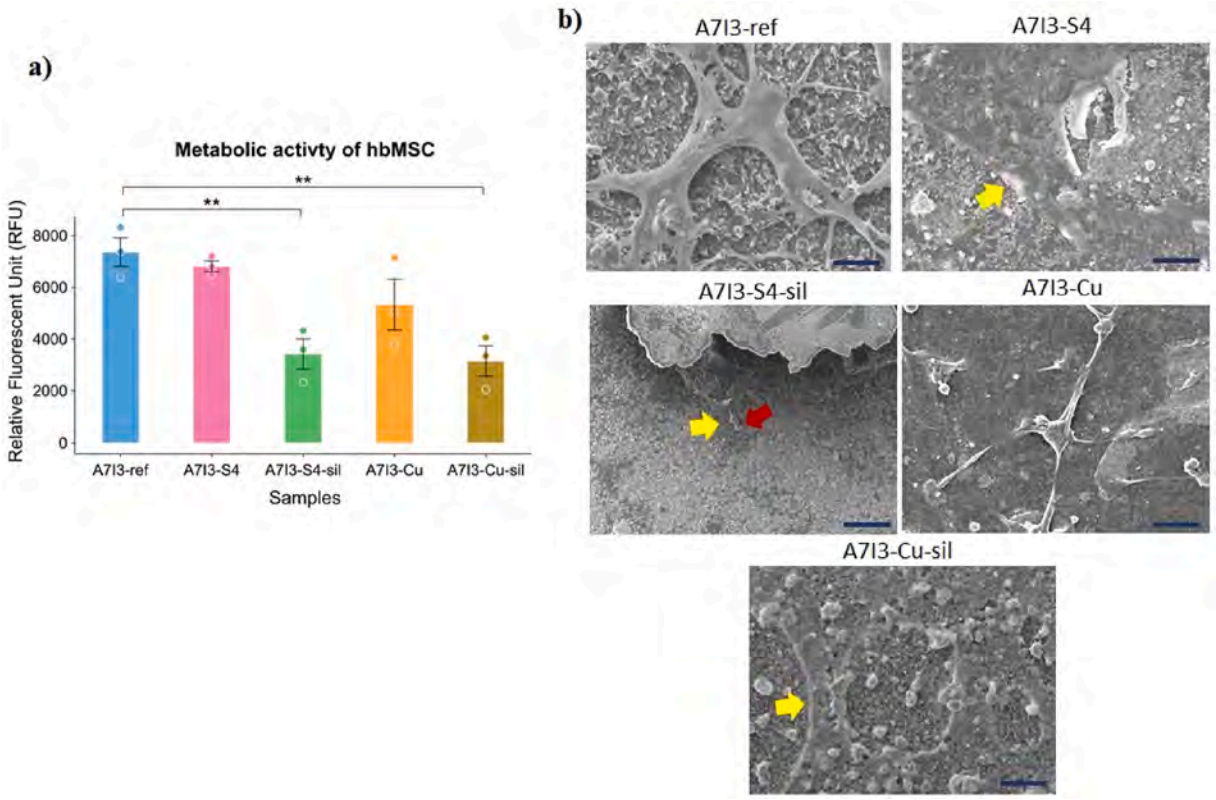
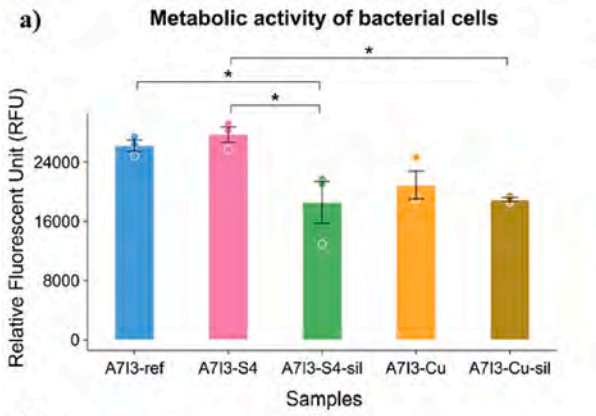


Fig. 11. *In vitro* cytocompatibility evaluation of samples (A7I3-ref, A7I3–S4, A7I3–S4sil, A7I3–Cu, and A7I3–Cu-sil) with hbMSC cells for 24 h at 37 °C. a) Metabolic activity of the surface-attached cells; b) SEM images, with yellow arrows indicating spread cells on the surface and red arrows showing non-attached cells; ** indicates $p < 0.01$; Scale bar = 50 μm.



b)

Viable surface-adhered bacterial colonies count

Name of the samples	Number of colonies ($\times 5\times10^6$)	Reduction (%)
A7I3-ref	3.5 (±0.7)	control
A7I3-S4	3.5 (±0.7)	0
A7I3-S4-sil	1.5 (±2)	57
A7I3-Cu	1.5 (±0.7)	57
A7I3-Cu-sil	1.5 (±2)	57

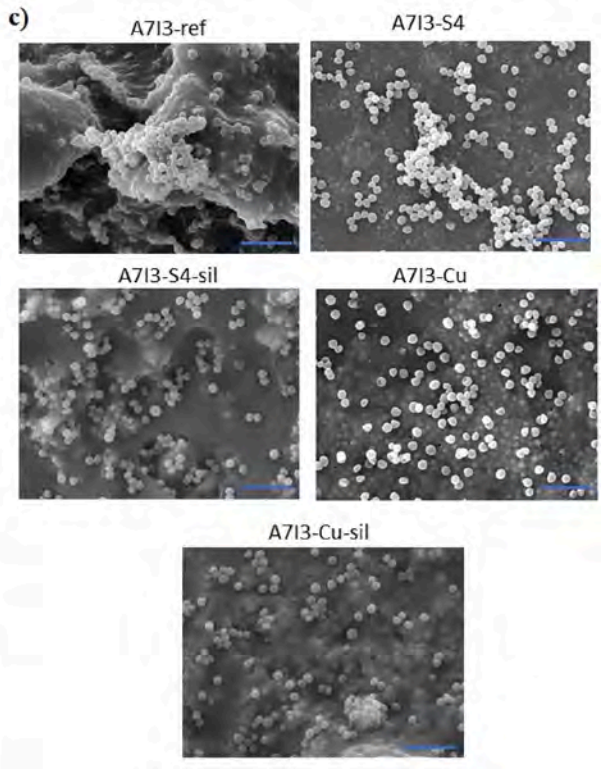
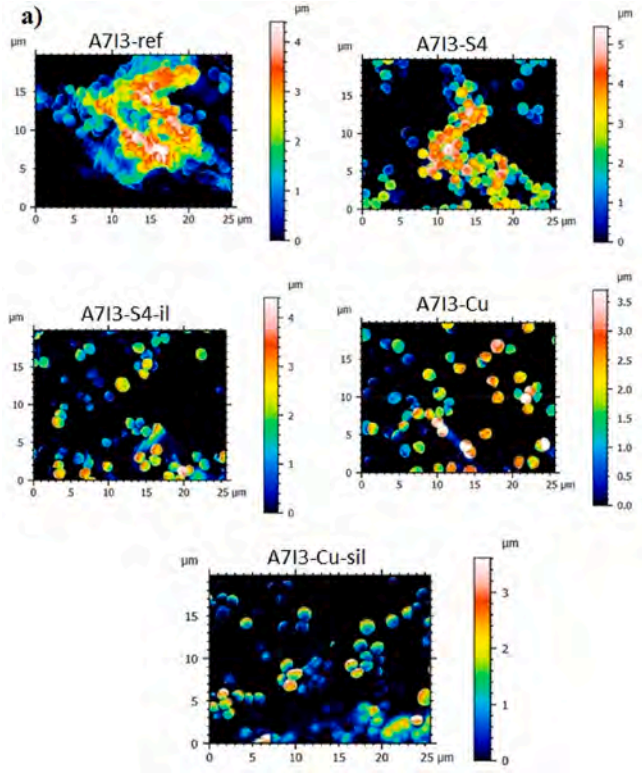


Fig. 12. *In vitro* antibacterial evaluation of samples (A7I3-ref, A7I3–S4, A7I3–S4sil, A7I3–Cu, and A7I3–Cu-sil) against *S. aureus* after 24 h of incubation at 37 °C, following the ISO 22196 protocol. a) Metabolic activity of the surface-adhered bacterial cells; b) CFU counting indicating the number of viable surface-adhered bacterial cells, $p < 0.05$ showed by *; c) SEM images; scale bar = 5 μm.



b)

Name of the samples	Occupied area (%)	Z-maximum (µm)
A7I3-ref	13	4.4
A7I3-S4	13.7	4.5
A7I3-S4-sil	9	3
A7I3-Cu	8	2.5
A7I3-Cu-sil	8.4	2.5

Fig. 13. Evaluation of bacterial aggregations thickness and occupied surface area (%) by bacterial cells. a) 3D-reconstructed SEM images using SMILE VIEW™ (MAP8.2.9621) software; b) Calculation of occupied area (%) and Z-maximum height using SMILE VIEW and ImageJ software, respectively.

surfaces, Cu ions can interfere with their metabolism, disturbing the bacterial cell wall, producing reactive oxygen species (ROS), and disturbing enzyme activity, leading to toxicity [103]. As reported in previous literature, Cu-doped BGs (Cu-SBA3) have demonstrated antibacterial activity against *S. aureus* Multi-drug resistance after 24 h [104].

The biological evaluation of the treated samples–using silanization (A7I3–S4-sil), Cu doping(A7I3–Cu), and a binary combination (A7I3–Cu-sil)–showed a promising reduction in the formation of bacterial aggregations on their surfaces. However, the cytocompatibility of these surfaces revealed a low tendency for cell attachment, probably due to changes in surface wettability, specially after silanization process. Improving surface characteristics to enhance cell compatibility can be considered as the next step of this project.

4. Conclusions

This study successfully demonstrated the development and characterisation of photo-curable, biobased resin reinforced with bioactive glasses (BGs) for potential tissue engineering applications. The BGs were modified by adding Cu ions to enhance antibacterial properties and subjected to silanization to improve mechanical strength. The silanization process successfully enhanced the compatibility of BGs with the photo-curable matrix, resulting in an enhanced elastic modulus and a 35 % increase in stress at break for both types of BGs tested while maintaining unvaried elongation at break.

The bioactivity of the scaffolds was validated through immersion in simulated body fluid (SBF), which demonstrated hydroxyapatite (HAp) formation, particularly in the samples containing Cu-doped BGs. This confirms the potential of these materials to support bone regeneration. The biological evaluation of the samples, including cytocompatibility and antibacterial assessment, demonstrated reduced metabolic activity and approximately 57 % fewer surface-adhered bacterial cells for the functionalized samples with silanization, Cu, and a combination of Cu and silanization, compared to the control sample (A7I3-ref) and A7I3–S4. These results were confirmed by SEM images, which showed a reduction in occupied surface area by bacteria and Z-maximum on the surfaces of A7I3-sil, A7I3–Cu, and A7I3–Cu-sil. However, the treated samples did not exhibit highly cell-friendly surfaces, likely due to changes in wettability following silanization. Improving their surface characteristics to enhance cell attachment can be considered for further experimental steps.

Overall, this study highlights the potential of these biobased and photo-curable resins reinforced with silanized BGs as optimal materials for 3D-printed bone scaffolds. The combination of mechanical strength, bioactivity and sustainability suggests that the materials could play a crucial role in the future of tissue engineering, providing a green alternative to fossil-based scaffolds while maintaining biocompatibility and promoting effective bone regeneration.

CRediT authorship contribution statement

Matteo Bergoglio: Writing – original draft, Visualization, Methodology, Investigation. **Ziba Najmi:** Writing – review & editing, Methodology, Investigation. **Andrea Cochis:** Writing – review & editing, Resources. **Marta Miola:** Writing – review & editing, Supervision, Resources, Conceptualization. **Enrica Vernè:** Writing – review & editing, Conceptualization. **Marco Sangermano:** Writing – review & editing, Supervision, Resources, Conceptualization.

Funding sources

This paper is part of a project that has received funding from the European Union's Horizon 2020 research and innovation program under the Marie Skłodowska-Curie grant agreement, No 101085759 (SURE-Poly).

Declaration of competing interest

The authors declare that they have no known competing financial interests or personal relationships that could have appeared to influence the work reported in this paper.

Data availability

Data will be made available on request.

References

[1] C.R.M. Black, V. Goriainov, D. Gibbs, J. Kanczler, R.S. Tare, R.O.C. Oreffo, Bone tissue engineering, Curr Mol Biol Rep 1 (2015) 132–140, https://doi.org/10.1007/s40610-015-0022-2.

[2] T. Kokubo, H.-M. Kim, M. Kawashita, Novel bioactive materials with different mechanical properties, Biomaterials 24 (2003) 2161–2175, https://doi.org/10.1016/S0142-9612(03)00044-9.

[3] T.-J. Cho, L.C. Gerstenfeld, T.A. Einhorn, Differential temporal expression of members of the transforming growth factor β superfamily during murine fracture healing, J. Bone Miner. Res. 17 (2002) 513–520, https://doi.org/10.1359/jbmr.2002.17.3.513.

[4] C. Ferguson, E. Alpern, T. Miclau, J.A. Helms, Does adult fracture repair recapitulate embryonic skeletal formation? Mech. Dev. 87 (1999) 57–66, https://doi.org/10.1016/S0925-4773(99)00142-2.

[5] L. Audig??, D. Griffin, M. Bhandari, J. Kellam, T.P. R??edi, Path analysis of factors for delayed healing and nonunion in 416 operatively treated tibial shaft fractures, Clin Orthop Relat Res NA (2005) 221–232, https://doi.org/10.1097/01.blo.0000163836.66906.74.

[6] A. Motameni, İ.S. Çardaklı, R. Gürbüz, A.Z. Alshemary, M. Razavi, Ö. C. Farukoğlu, Bioglass-polymer composite scaffolds for bone tissue regeneration: a review of current trends, International Journal of Polymeric Materials and Polymeric Biomaterials (2023) 1–20, https://doi.org/10.1080/00914037.2023.2186864.

[7] H. Qu, H. Fu, Z. Han, Y. Sun, Biomaterials for bone tissue engineering scaffolds: a review, RSC Adv. 9 (2019) 26252–26262, https://doi.org/10.1039/C9RA05214C.

[8] A.M. Deliormanli, M. Ensoylu, G. Almisned, H.O. Tekin, Two-dimensional molybdenum disulfide/polymer-coated bioactive glass scaffolds for tissue engineering: fabrication, structural, mechanical, bioactivity, and radiation interaction properties, Ceram. Int. 49 (2023) 22861–22874, https://doi.org/10.1016/j.ceramint.2023.04.110.

[9] W. Cao, L.L. Hench, Bioactive materials, Ceram. Int. 22 (1996) 493–507, https://doi.org/10.1016/0272-8842(95)00126-3.

[10] L. Drago, M. Toscano, M. Bottagisio, Recent evidence on bioactive glass antimicrobial and antibiofilm activity: a mini-review, Materials 11 (2018) 326, https://doi.org/10.3390/ma11020326.

[11] J. Rivadeneira, A. Gorustovich, Bioactive glasses as delivery systems for antimicrobial agents, J. Appl. Microbiol. 122 (2017) 1424–1437, https://doi.org/10.1111/jam.13393.

[12] R. Sergi, D. Bellucci, V. Cannillo, A review of bioactive glass/natural polymer composites: state of the art, Materials 13 (2020) 5560, https://doi.org/10.3390/ma13235560.

[13] J.P. Rodríguez, S. Ríos, M. González, Modulation of the proliferation and differentiation of human mesenchymal stem cells by copper, J. Cell. Biochem. 85 (2002) 92–100, https://doi.org/10.1002/jcb.10111.

[14] K. Malachová, P. Praus, Z. Rybková, O. Kozák, Antibacterial and antifungal activities of silver, copper and zinc montmorillonites, Appl. Clay Sci. 53 (2011) 642–645, https://doi.org/10.1016/j.clay.2011.05.016.

[15] S. Kargozar, M. Mozafari, S. Ghodrat, E. Fiume, F. Baino, Copper-containing bioactive glasses and glass-ceramics: from tissue regeneration to cancer therapeutic strategies, Mater. Sci. Eng. C 121 (2021) 111741, https://doi.org/10.1016/j.msec.2020.111741.

[16] B. Cao, Y. Zheng, T. Xi, C. Zhang, W. Song, K. Burugapalli, H. Yang, Y. Ma, Concentration-dependent cytotoxicity of copper ions on mouse fibroblasts in vitro: effects of copper ion release from TCu380A vs TCu220C intra-uterine devices, Biomed. Microdevices 14 (2012) 709–720, https://doi.org/10.1007/s10544-012-9651-x.

[17] L.L. Hench, The story of Bioglass, J. Mater. Sci. Mater. Med. 17 (2006) 967–978, https://doi.org/10.1007/s10856-006-0432-z.

[18] J.R. Jones, Review of bioactive glass: from Hench to hybrids, Acta Biomater. 9 (2013) 4457–4486, https://doi.org/10.1016/j.actbio.2012.08.023.

[19] M. Mohammadi Zerankeshi, R. Bakhshi, R. Alizadeh, Polymer/metal composite 3D porous bone tissue engineering scaffolds fabricated by additive manufacturing techniques: a review, Bioprinting 25 (2022) e00191, https://doi.org/10.1016/j.bprint.2022.e00191.

[20] J.M. Taboas, R.D. Maddox, P.H. Krebsbach, S.J. Hollister, Indirect solid free form fabrication of local and global porous, biomimetic and composite 3D polymer-ceramic scaffolds, Biomaterials 24 (2003) 181–194, https://doi.org/10.1016/S0142-9612(02)00276-4.

[21] J.R. Venugopal, S. Low, A.T. Choon, A.B. Kumar, S. Ramakrishna, Nanobioengineered electrospun composite nanofibers and osteoblasts for bone regeneration, Artif. Organs 32 (2008) 388–397, https://doi.org/10.1111/j.1525-1594.2008.00557.x.

[22] P. Szymczyk-Ziółkowska, M.B. Łabowska, J. Detyna, I. Michalak, P. Gruber, A review of fabrication polymer scaffolds for biomedical applications using additive manufacturing techniques, Biocybern. Biomed. Eng. 40 (2020) 624–638, https://doi.org/10.1016/j.bbe.2020.01.015.

[23] A. Martelli, D. Bellucci, V. Cannillo, Additive manufacturing of polymer/bioactive glass scaffolds for regenerative medicine: a review, Polymers 15 (2023) 2473, https://doi.org/10.3390/polym15112473.

[24] P. Szymczyk-Ziółkowska, M.B. Łabowska, J. Detyna, I. Michalak, P. Gruber, A review of fabrication polymer scaffolds for biomedical applications using additive manufacturing techniques, Biocybern. Biomed. Eng. 40 (2020) 624–638, https://doi.org/10.1016/j.bbe.2020.01.015.

[25] J. Liu, L. Sun, W. Xu, Q. Wang, S. Yu, J. Sun, Current advances and future perspectives of 3D printing natural-derived biopolymers, Carbohydr. Polym. 207 (2019) 297–316, https://doi.org/10.1016/j.carbpol.2018.11.077.

[26] S.J. Trenfield, C.M. Madla, A.W. Basit, S. Gaisford, The Shape of Things to Come: Emerging Applications of 3D Printing in Healthcare, 2018, pp. 1–19, https://doi.org/10.1007/978-3-319-90755-0_1.

[27] J. Yao, M. Morsali, A. Moreno, M.H. Sipponen, M. Hakkarainen, Lignin nanoparticle-enhanced biobased resins for digital light processing 3D printing: towards high resolution and tunable mechanical properties, Eur. Polym. J. 194 (2023) 112146, https://doi.org/10.1016/j.eurpolymj.2023.112146.

[28] R. Chaudhary, P. Fabbri, E. Leoni, F. Mazzanti, R. Akbari, C. Antonini, Additive manufacturing by digital light processing: a review, Progress in Additive Manufacturing 8 (2023) 331–351, https://doi.org/10.1007/s40964-022-00336-0.

[29] K.A. van Kampen, R.G. Scheuring, M.L. Terpstra, R. Levato, J. Groll, J. Malda, C. Mota, L. Moroni, Biofabrication: from additive manufacturing to bioprinting, in: R.L. Reis (Ed.), Encyclopedia of Tissue Engineering and Regenerative Medicine, Academic Press, Oxford, 2019, pp. 41–55, https://doi.org/10.1016/B978-0-12-801238-3.11118-3.

[30] A. Luongo, V. Falster, M.B. Doest, M.M. Ribo, E.R. Eiriksson, D.B. Pedersen, J. R. Frisvad, Microstructure control in 3D printing with digital light processing, Comput. Graph. Forum 39 (2020) 347–359, https://doi.org/10.1111/cgf.13807.

[31] Q. Chen, C. Zhu, G.A. Thouas, Progress and challenges in biomaterials used for bone tissue engineering: bioactive glasses and elastomeric composites, Prog Biomater 1 (2012) 2, https://doi.org/10.1186/2194-0517-1-2.

[32] A. Martelli, D. Bellucci, V. Cannillo, Additive manufacturing of polymer/bioactive glass scaffolds for regenerative medicine: a review, Polymers 15 (2023) 2473, https://doi.org/10.3390/polym15112473.

[33] A. Davoudinejad, Vat photopolymerization methods in additive manufacturing, in: Addit Manuf, Elsevier, 2021, pp. 159–181, https://doi.org/10.1016/B978-0-12-818411-0.00007-0.

[34] M. Sangermano, M. Bergoglio, S. Schögl, Biobased vitrimeric epoxy networks, Macromol. Mater. Eng. (2023), https://doi.org/10.1002/mame.202300371.

[35] M. Porcarello, S. Bonardd, G. Kortaberria, Y. Miyaji, K. Matsukawa, M. Sangermano, 3D printing of electrically conductive objects with biobased polyglycerol acrylic monomers, ACS Appl. Polym. Mater. 6 (2024) 2868–2876, https://doi.org/10.1021/acsapm.3c03073.

[36] M. Bergoglio, D. Reisinger, S. Schlögl, T. Griesser, M. Sangermano, Sustainable bio-based UV-cured epoxy vitrimer from Castor oil, Polymers 15 (2023) 1024, https://doi.org/10.3390/polym15041024.

[37] M. Bergoglio, Z. Najmi, A. Cochis, M. Miola, E. Vernè, M. Sangermano, UV-cured bio-based acrylated soybean oil scaffold reinforced with bioactive glasses, Polymers 15 (2023) 4089, https://doi.org/10.3390/polym15204089.

[38] M. Bergoglio, G. Palazzo, D. Reisinger, M. Porcarello, G. Kortaberria, S. Schlögl, M. Sangermano, Cationic UV-curing of bio-based epoxidized castor oil vitrimers with electrically conductive properties, React. Funct. Polym. 200 (2024) 105936, https://doi.org/10.1016/j.reactfunctpolym.2024.105936.

[39] M. Bergoglio, E. Rossegger, S. Schlögl, T. Griesser, C. Waly, F. Arbeiter, M. Sangermano, Multi-material 3D printing of biobased epoxy resins, Polymers 16 (2024) 1510, https://doi.org/10.3390/polym16111510.

[40] A. Bagheri, J. Jin, Photopolymerization in 3D printing, ACS Appl. Polym. Mater. 1 (2019) 593–611, https://doi.org/10.1021/acsapm.8b00165.

[41] L. Pezzana, G. Melilli, N. Guigo, N. Sbirrazzuoli, M. Sangermano, Cross-linking of biobased monofunctional furan epoxy monomer by two steps process, UV irradiation and thermal treatment, Macromol. Chem. Phys. 224 (2023), https://doi.org/10.1002/macp.202200012.

[42] L. Pezzana, G. Melilli, P. Delliere, D. Moraru, N. Guigo, N. Sbirrazzuoli, M. Sangermano, Thiol-ene biobased networks: furan allyl derivatives for green coating applications, Prog. Org. Coating 173 (2022), https://doi.org/10.1016/j.porgcoat.2022.107203.

[43] S. Subramaniyan, M. Bergoglio, M. Sangermano, M. Hakkarainen, Vanillin-derived thermally reprocessable and chemically recyclable schiff-base epoxy thermosets, Global Challenges 7 (2023), https://doi.org/10.1002/gch2.202200234.

[44] M. Bergoglio, D. Reisinger, S. Schlögl, T. Griesser, M. Sangermano, Sustainable bio-based UV-cured epoxy vitrimer from Castor oil, Polymers 15 (2023), https://doi.org/10.3390/polym15041024.

[45] C. Mendes-Felipe, R. Cofano, A. Garcia, M. Sangermano, S. Lanceros-Mendez, Photocurable 3D printed anisotropic electrically conductive materials based on bio-renewable composites, Addit. Manuf. 78 (2023) 103867, https://doi.org/10.1016/j.addma.2023.103867.

[46] V.S.D. Voet, J. Guit, K. Loos, Sustainable photopolymers in 3D printing: a review on biobased, biodegradable, and recyclable alternatives, Macromol. Rapid Commun. 42 (2021), https://doi.org/10.1002/marc.202000475.
[47] M. Layani, X. Wang, S. Magdassi, Novel materials for 3D printing by photopolymerization, Adv. Mater. 30 (2018), https://doi.org/10.1002/adma.201706344.
[48] L. Pezzana, R. Wolff, J. Stampfl, R. Liska, M. Sangermano, High temperature vat photopolymerization 3D printing of fully bio-based composites: green vegetable oil epoxy matrix & bio-derived filler powder, Addit. Manuf. 79 (2024) 103929, https://doi.org/10.1016/j.addma.2023.103929.
[49] M. Bergoglio, E. Rossegger, S. Schlögl, T. Griesser, C. Waly, F. Arbeiter, M. Sangermano, Multi-material 3D printing of biobased epoxy resins, Polymers 16 (2024) 1510, https://doi.org/10.3390/polym16111510.
[50] M. Bergoglio, Z. Najmi, A. Cochis, M. Miola, E. Vernè, M. Sangermano, UV-cured bio-based acrylated soybean oil scaffold reinforced with bioactive glasses, Polymers 15 (2023) 4089, https://doi.org/10.3390/polym15204089.
[51] L. Pierau, C. Elian, J. Akimoto, Y. Ito, S. Caillol, D.-L. Versace, Bio-sourced monomers and cationic photopolymerization–The green combination towards eco-friendly and non-toxic materials, Prog. Polym. Sci. 127 (2022) 101517, https://doi.org/10.1016/j.progpolymsci.2022.101517.
[52] X. Chen, S. Chen, Z. Xu, J. Zhang, M. Miao, D. Zhang, Degradable and recyclable bio-based thermoset epoxy resins, Green Chem. 22 (2020) 4187–4198, https://doi.org/10.1039/D0GC01250E.
[53] A. Gandini, Polymers from renewable resources: a challenge for the future of macromolecular materials, Macromolecules 41 (2008) 9491–9504, https://doi.org/10.1021/ma801735u.
[54] A. Gandini, The irruption of polymers from renewable resources on the scene of macromolecular science and technology, Green Chem. 13 (2011) 1061, https://doi.org/10.1039/c0gc00789g.
[55] R. Mustapha, A.R. Rahmat, R. Abdul Majid, S.N.H. Mustapha, Vegetable oil-based epoxy resins and their composites with bio-based hardener: a short review, Polymer-Plastics Technology and Materials 58 (2019) 1311–1326, https://doi.org/10.1080/25740881.2018.1563119.
[56] S. Miao, P. Wang, Z. Su, S. Zhang, Vegetable-oil-based polymers as future polymeric biomaterials, Acta Biomater. 10 (2014) 1692–1704, https://doi.org/10.1016/j.actbio.2013.08.040.
[57] S. Miao, W. Zhu, N.J. Castro, M. Nowicki, X. Zhou, H. Cui, J.P. Fisher, L.G. Zhang, 4D printing smart biomedical scaffolds with novel soybean oil epoxidized acrylate, Sci. Rep. 6 (2016) 27226, https://doi.org/10.1038/srep27226.
[58] D. Mondal, A. Srinivasan, P. Comeau, Y.-C. Toh, T.L. Willett, Acrylated epoxidized soybean oil/hydroxyapatite-based nanocomposite scaffolds prepared by additive manufacturing for bone tissue engineering, Mater. Sci. Eng. C 118 (2021) 111400, https://doi.org/10.1016/j.msec.2020.111400.
[59] A. Barkane, O. Platnieks, M. Jurinovs, S. Kasetaite, J. Ostrauskaite, S. Gaidukovs, Y. Habibi, UV-light curing of 3D printing inks from vegetable oils for stereolithography, Polymers 13 (2021) 1195, https://doi.org/10.3390/polym13081195.
[60] A. Barkane, O. Platnieks, M. Jurinovs, S. Gaidukovs, Thermal stability of UV-cured vegetable oil epoxidized acrylate-based polymer system for 3D printing application, Polym. Degrad. Stabil. 181 (2020) 109347, https://doi.org/10.1016/j.polymdegradstab.2020.109347.
[61] C. Vazquez-Martel, L. Becker, W.V. Liebig, P. Elsner, E. Blasco, Vegetable oils as sustainable inks for additive manufacturing: a comparative study, ACS Sustain. Chem. Eng. 9 (2021) 16840–16848, https://doi.org/10.1021/acssuschemeng.1c06784.
[62] C. Noè, A. Cosola, C. Tonda-Turo, R. Sesana, C. Delprete, A. Chiappone, M. Hakkarainen, M. Sangermano, DLP-printable fully biobased soybean oil composites, Polymer (Guildf) 247 (2022) 124779, https://doi.org/10.1016/j.polymer.2022.124779.
[63] D. Mondal, A. Srinivasan, P. Comeau, Y.-C. Toh, T.L. Willett, Acrylated epoxidized soybean oil/hydroxyapatite-based nanocomposite scaffolds prepared by additive manufacturing for bone tissue engineering, Mater. Sci. Eng. C 118 (2021) 111400, https://doi.org/10.1016/j.msec.2020.111400.
[64] F. Courtecuisse, A. Belbakra, C. Croutxé-Barghorn, X. Allonas, C. Dietlin, Zirconium complexes to overcome oxygen inhibition in free-radical photopolymerization of acrylates: kinetic, mechanism, and depth profiling, J. Polym. Sci. Polym. Chem. 49 (2011) 5169–5175, https://doi.org/10.1002/pola.24984.
[65] J. Steindl, T. Koch, N. Moszner, C. Gorsche, Silane–acrylate chemistry for regulating network formation in radical photopolymerization, Macromolecules 50 (2017) 7448–7457, https://doi.org/10.1021/acs.macromol.7b01399.
[66] A. Prasad, S. Bhasney, V. Katiyar, M. Ravi Sankar, Biowastes processed hydroxyapatite filled poly (lactic acid) bio-composite for open reduction internal fixation of small bones, Mater. Today Proc. 4 (2017) 10153–10157, https://doi.org/10.1016/j.matpr.2017.06.339.
[67] A. Prasad, M.R. Sankar, V. Katiyar, State of art on solvent casting particulate leaching method for orthopedic ScaffoldsFabrication, Mater. Today Proc. 4 (2017) 898–907, https://doi.org/10.1016/j.matpr.2017.01.101.
[68] B. Huang, G. Caetano, C. Vyas, J. Blaker, C. Diver, P. Bártolo, Polymer-ceramic composite scaffolds: the effect of hydroxyapatite and β-tri-Calcium phosphate, Materials 11 (2018) 129, https://doi.org/10.3390/ma11010129.
[69] J.J. Blaker, V. Maquet, R. Jérôme, A.R. Boccaccini, S.N. Nazhat, Mechanical properties of highly porous PDLLA/Bioglass® composite foams as scaffolds for bone tissue engineering, Acta Biomater. 1 (2005) 643–652, https://doi.org/10.1016/j.actbio.2005.07.003.
[70] S. Jain, R. Gujjala, P. Abdul Azeem, S. Ojha, R.K. Samudrala, A review on mechanical and In-vitro studies of polymer reinforced bioactive glass-scaffolds and their fabrication techniques, Ceram. Int. 48 (2022) 5908–5921, https://doi.org/10.1016/j.ceramint.2021.11.206.
[71] Z. Raszewski, K. Chojnacka, J. Kulbacka, M. Mikulewicz, Mechanical properties and biocompatibility of 3D printing acrylic material with bioactive components, J. Funct. Biomater. 14 (2022) 13, https://doi.org/10.3390/jfb14010013.
[72] Y. Ding, X. Liu, J. Zhang, Z. Lv, X. Meng, Z. Yuan, T. Long, Y. Wang, 3D printing polylactic acid polymer-bioactive glass loaded with bone cement for bone defect in weight-bearing area, Front. Bioeng. Biotechnol. 10 (2022), https://doi.org/10.3389/fbioe.2022.947521.
[73] E. Schätzlein, C. Kicker, N. Söhling, U. Ritz, J. Neijhoft, D. Henrich, J. Frank, I. Marzi, A. Blaeser, 3D-Printed PLA-bioglass scaffolds with controllable calcium release and MSC adhesion for bone tissue engineering, Polymers 14 (2022) 2389, https://doi.org/10.3390/polym14122389.
[74] J.J. Blaker, V. Maquet, A.R. Boccaccini, R. Jérôme, A. Bismarck, Wetting of bioactive glass surfaces by poly(α-hydroxyacid) melts: interaction between Bioglass® and biodegradable polymers, E-Polymers 5 (2005), https://doi.org/10.1515/epoly.2005.5.1.248.
[75] D. Vukajlovic, J. Parker, O. Bretcanu, K. Novakovic, Chitosan based polymer/bioglass composites for tissue engineering applications, Mater. Sci. Eng. C 96 (2019) 955–967, https://doi.org/10.1016/j.msec.2018.12.026.
[76] K. Zhang, Y. Ma, L.F. Francis, Porous polymer/bioactive glass composites for soft-to-hard tissue interfaces, J. Biomed. Mater. Res. 61 (2002) 551–563, https://doi.org/10.1002/jbm.10227.
[77] R. Ravarian, X. Zhong, M. Barbeck, S. Ghanaati, C.J. Kirkpatrick, C.M. Murphy, A. Schindeler, W. Chrzanowski, F. Dehghani, Nanoscale chemical interaction enhances the physical properties of bioglass composites, ACS Nano 7 (2013) 8469–8483, https://doi.org/10.1021/nn402157n.
[78] T.-C. Nguyen, T.-D. Nguyen, D.-T. Vu, D.-P. Dinh, A.-H. Nguyen, T.-N.-L. Ly, P.-H. Dao, T.-L. Nguyen, L.-G. Bach, H. Thai, Modification of titanium dioxide nanoparticles with 3-(Trimethoxysilyl)propyl methacrylate silane coupling agent, J. Chem. 2020 (2020) 1–10, https://doi.org/10.1155/2020/1381407.
[79] P.H. Dao, T.C. Nguyen, T.L. Phung, T.D. Nguyen, A.H. Nguyen, T.N.L. Vu, Q. T. Vu, D.H. Vu, T.K.N. Tran, H. Thai, Assessment of some characteristics and properties of zirconium dioxide nanoparticles modified with 3-(trimethoxysilyl) propyl methacrylate silane coupling agent, J. Chem. 2021 (2021) 1–10, https://doi.org/10.1155/2021/9925355.
[80] A.A. El-Rashidy, G. Waly, A. Gad, A.A. Hashem, P. Balasubramanian, S. Kaya, A. R. Boccaccini, I. Sami, Preparation and in vitro characterization of silver-doped bioactive glass nanoparticles fabricated using a sol-gel process and modified Stöber method, J. Non-Cryst. Solids 483 (2018) 26–36, https://doi.org/10.1016/j.jnoncrysol.2017.12.044.
[81] T. Kokubo, H. Takadama, How useful is SBF in predicting in vivo bone bioactivity? Biomaterials 27 (2006) 2907–2915, https://doi.org/10.1016/j.biomaterials.2006.01.017.
[82] T. Kokubo, H. Takadama, How useful is SBF in predicting in vivo bone bioactivity? Biomaterials 27 (2006) 2907–2915, https://doi.org/10.1016/j.biomaterials.2006.01.017.
[83] M.U. Okwu, M. Olley, A.O. Akpoka, O.E. Izevbuwa, Methicillin-resistant Staphylococcus aureus (MRSA) and anti-MRSA activities of extracts of some medicinal plants: a brief review, AIMS Microbiol 5 (2019) 117–137, https://doi.org/10.3934/microbiol.2019.2.117.
[84] P.H. Dao, T.C. Nguyen, T.L. Phung, T.D. Nguyen, A.H. Nguyen, T.N.L. Vu, Q. T. Vu, D.H. Vu, T.K.N. Tran, H. Thai, Assessment of some characteristics and properties of zirconium dioxide nanoparticles modified with 3-(trimethoxysilyl) propyl methacrylate silane coupling agent, J. Chem. 2021 (2021) 1–10, https://doi.org/10.1155/2021/9925355.
[85] T.-C. Nguyen, T.-D. Nguyen, D.-T. Vu, D.-P. Dinh, A.-H. Nguyen, T.-N.-L. Ly, P.-H. Dao, T.-L. Nguyen, L.-G. Bach, H. Thai, Modification of titanium dioxide nanoparticles with 3-(Trimethoxysilyl)propyl methacrylate silane coupling agent, J. Chem. 2020 (2020) 1–10, https://doi.org/10.1155/2020/1381407.
[86] M. Bergoglio, Z. Najmi, A. Cochis, M. Miola, E. Vernè, M. Sangermano, UV-cured bio-based acrylated soybean oil scaffold reinforced with bioactive glasses, Polymers 15 (2023) 4089, https://doi.org/10.3390/polym15204089.
[87] S. Liu, L. Mo, G. Bi, S. Chen, D. Yan, J. Yang, Y.-G. Jia, L. Ren, DLP 3D printing porous β-tricalcium phosphate scaffold by the use of acrylate/ceramic composite slurry, Ceram. Int. 47 (2021) 21108–21116, https://doi.org/10.1016/j.ceramint.2021.04.114.
[88] E. Rossegger, R. Höller, K. Hrbinič, M. Sangermano, T. Griesser, S. Schlögl, 3D printing of soft magnetoactive devices with thiol-click photopolymer composites, Adv. Eng. Mater. 25 (2023) 2200749, https://doi.org/10.1002/adem.202200749.
[89] Y. Yao, N. Sha, Z. Zhao, Highly concentrated hydroxyapatite suspension for DLP printing, IOP Conf. Ser. Mater. Sci. Eng. 678 (2019) 012016, https://doi.org/10.1088/1757-899X/678/1/012016.
[90] Y. Yao, N. Sha, Z. Zhao, Highly concentrated hydroxyapatite suspension for DLP printing, IOP Conf. Ser. Mater. Sci. Eng. 678 (2019) 012016, https://doi.org/10.1088/1757-899X/678/1/012016.
[91] C. Hinczewski, S. Corbel, T. Chartier, Ceramic suspensions suitable for stereolithography, J. Eur. Ceram. Soc. 18 (1998) 583–590, https://doi.org/10.1016/S0955-2219(97)00186-6.
[92] F.P.W. Melchels, J. Feijen, D.W. Grijpma, A poly(d,l-lactide) resin for the preparation of tissue engineering scaffolds by stereolithography, Biomaterials 30 (2009) 3801–3809, https://doi.org/10.1016/j.biomaterials.2009.03.055.

[93] R.J. Mondschein, A. Kanitkar, C.B. Williams, S.S. Verbridge, T.E. Long, Polymer structure-property requirements for stereolithographic 3D printing of soft tissue engineering scaffolds, Biomaterials 140 (2017) 170–188, https://doi.org/10.1016/j.biomaterials.2017.06.005.

[94] I.L. de Camargo, M.M. Morais, C.A. Fortulan, M.C. Branciforti, A review on the rheological behavior and formulations of ceramic suspensions for vat photopolymerization, Ceram. Int. 47 (2021) 11906–11921, https://doi.org/10.1016/j.ceramint.2021.01.031.

[95] W.L. Tham, W.S. Chow, Z.A.M. Ishak, The effect of 3-(trimethoxysilyl) propyl methacrylate on the mechanical, thermal, and morphological properties of poly (methyl methacrylate)/hydroxyapatite composites, J. Appl. Polym. Sci. 118 (2010) 218–228, https://doi.org/10.1002/app.32111.

[96] S. Raynaud, E. Champion, D. Bernache-Assollant, Calcium phosphate apatites with variable Ca/P atomic ratio II. Calcination and sintering, Biomaterials 23 (2002) 1073–1080, https://doi.org/10.1016/S0142-9612(01)00219-8.

[97] S. Shahabi, F. Najafi, A. Majdabadi, T. Hooshmand, M. Haghbin Nazarpak, B. Karimi, S.M. Fatemi, Effect of gamma irradiation on structural and biological properties of a PLGA-PEG-hydroxyapatite composite, Sci. World J. 2014 (2014) 1–9, https://doi.org/10.1155/2014/420616.

[98] J. Bejarano, P. Caviedes, H. Palza, Sol–gel synthesis and *in vitro* bioactivity of copper and zinc-doped silicate bioactive glasses and glass-ceramics, Biomed. Mater. 10 (2015) 025001, https://doi.org/10.1088/1748-6041/10/2/025001.

[99] S. Kapoor, D. Brazete, I.C. Pereira, G. Bhatia, M. Kaur, L.F. Santos, D. Banerjee, A. Goel, J.M.F. Ferreira, Impact of transition metal ions on the structure and bioactivity of alkali-free bioactive glasses, J. Non-Cryst. Solids 506 (2019) 98–108, https://doi.org/10.1016/j.jnoncrysol.2018.12.003.

[100] S. Kargozar, M. Mozafari, S. Ghodrat, E. Fiume, F. Baino, Copper-containing bioactive glasses and glass-ceramics: from tissue regeneration to cancer therapeutic strategies, Mater. Sci. Eng. C 121 (2021) 111741, https://doi.org/10.1016/j.msec.2020.111741.

[101] T. Ramesh, Osteogenic differentiation potential of human bone marrow-derived mesenchymal stem cells enhanced by <scp>bacoside-A</scp&gt, Cell Biochem. Funct. 39 (2021) 148–158, https://doi.org/10.1002/cbf.3596.

[102] M. Szafraniec, D. Barnat-Hunek, Evaluation of the contact angle and wettability of hydrophobised lightweight concrete with sawdust, Budownictwo i Architektura 19 (2020) 19–32, https://doi.org/10.35784/bud-arch.1644.

[103] B. Božić Cvijan, J. Korać Jačić, M. Bajčetić, The impact of copper ions on the activity of antibiotic drugs, Molecules 28 (2023) 5133, https://doi.org/10.3390/molecules28135133.

[104] M. Lallukka, M. Miola, Z. Najmi, A. Cochis, S. Spriano, L. Rimondini, E. Verné, Cu-doped bioactive glass with enhanced in vitro bioactivity and antibacterial properties, Ceram. Int. 50 (2024) 5091–5103, https://doi.org/10.1016/j.ceramint.2023.11.253.